

2014

# Nuclear subsurface explosion modeling and hydrodynamic fragmentation simulation of hazardous asteroids

Pavithra Dhanuka Premaratne  
*Iowa State University*

Follow this and additional works at: <https://lib.dr.iastate.edu/etd>

 Part of the [Aerospace Engineering Commons](#)

## Recommended Citation

Premaratne, Pavithra Dhanuka, "Nuclear subsurface explosion modeling and hydrodynamic fragmentation simulation of hazardous asteroids" (2014). *Graduate Theses and Dissertations*. 13852.  
<https://lib.dr.iastate.edu/etd/13852>

This Thesis is brought to you for free and open access by the Iowa State University Capstones, Theses and Dissertations at Iowa State University Digital Repository. It has been accepted for inclusion in Graduate Theses and Dissertations by an authorized administrator of Iowa State University Digital Repository. For more information, please contact [digirep@iastate.edu](mailto:digirep@iastate.edu).

**Nuclear subsurface explosion modeling and hydrodynamic fragmentation  
simulation of hazardous asteroids**

by

Pavithra Dhanuka Premaratne

A thesis submitted to the graduate faculty  
in partial fulfillment of the requirements for the degree of  
MASTER OF SCIENCE

Major: Aerospace Engineering

Program of Study Committee:

Bong Wie, Major Professor

John Basart

Ganesh Rajagopalan

Iowa State University

Ames, Iowa

2014

Copyright © Pavithra Dhanuka Premaratne, 2014. All rights reserved.

## DEDICATION

I would like to dedicate this thesis to my parents without whose support I would not have been able to complete this work. I would also like to thank my friends and family for their loving guidance and assistance during the writing of this work.

## TABLE OF CONTENTS

<b>LIST OF TABLES</b> . . . . .	iv
<b>LIST OF FIGURES</b> . . . . .	v
<b>ACKNOWLEDGEMENTS</b> . . . . .	vi
<b>ABSTRACT</b> . . . . .	vii
<b>CHAPTER 1. OVERVIEW</b> . . . . .	1
1.1 Introduction . . . . .	1
1.2 SPH method . . . . .	2
1.2.1 Formulation . . . . .	3
1.2.2 Kernel Function . . . . .	4
1.2.3 Artificial Viscosity . . . . .	5
1.2.4 Time Integration . . . . .	6
1.3 History of Hydrodynamic Modeling . . . . .	7
<b>CHAPTER 2. Simulation Capabilities</b> . . . . .	9
2.1 Material Modeling . . . . .	9
2.2 HAIV concept simulation . . . . .	11
2.3 Sensitivity Studies . . . . .	14
2.4 AUTODYN vs In House Algorithm . . . . .	20
2.4.1 AUTODYN . . . . .	20
2.4.2 Solver Capabilities . . . . .	21
2.4.3 SPH Solver Comparison . . . . .	23

<b>CHAPTER 3. Blast Simulation and Modeling</b> . . . . .	<b>25</b>
3.1 Initial Settings . . . . .	25
3.1.1 Energy Coupling Methods . . . . .	26
3.1.2 Material Modeling . . . . .	27
3.2 Algorithm Validation . . . . .	29
3.2.1 Detonation of 1D Bar of TNT (AUTODYN) . . . . .	29
3.2.2 Underwater Explosion Simulations (UNDEX) . . . . .	30
3.3 PRELIMINARY RESULTS AND ANALYSIS . . . . .	33
3.3.1 2D Planar Simulations (JWL) . . . . .	33
3.3.2 2D Planar Simulations (DED) . . . . .	35
3.3.3 2D Axial Symmetric Solver . . . . .	36
3.4 Conclusions . . . . .	38
<b>CHAPTER 4. Thermal Shield Development</b> . . . . .	<b>39</b>
4.1 Stage 1 . . . . .	39
4.2 Stage 2 . . . . .	41
4.3 Stage 3 . . . . .	43
4.3.1 Validation of Explicit Heat Diffusion . . . . .	44
4.4 Stage 4 . . . . .	46
4.5 Design Process - Example . . . . .	46
<b>CHAPTER 5. Whipple Shield Development</b> . . . . .	<b>50</b>
5.1 Ballistic Limit Equations (BLE) . . . . .	51
5.2 Validation of Whipple Shield Design Process . . . . .	53
5.3 Whipple Shield - Validation 2 . . . . .	55
5.3.1 Whipple Shield for HAIV . . . . .	57
<b>CHAPTER 6. Future Work</b> . . . . .	<b>58</b>
6.1 Blast Modeling . . . . .	58
6.1.1 Sod's Shock Tube . . . . .	59
6.1.2 Taylor-Sedov Blast Wave . . . . .	61

6.2 Thermal and Whipple Shield Development . . . . .	62
<b>BIBLIOGRAPHY</b> . . . . .	63
<b>BIBLIOGRAPHY</b> . . . . .	63

## LIST OF TABLES

Table 3.1	Shock equation of state properties . . . . .	29
Table 3.2	Tillotson equation of state properties . . . . .	34
Table 3.3	JWL equation of state properties . . . . .	34
Table 3.4	Subsurface vs contact - JWL . . . . .	35
Table 3.5	Subsurface vs contact (DED) . . . . .	36
Table 3.6	Subsurface vs contact - Axial symmetric . . . . .	36
Table 4.1	Material properties . . . . .	46
Table 4.2	Temperatures of each side . . . . .	48
Table 5.1	Shock EOS : Al-2024 and Al-1100 . . . . .	53
Table 5.2	Johnson-Cook : Al-2024 and Al-1100 . . . . .	54
Table 5.3	Whipple validation results . . . . .	56
Table 6.1	Ideal gas properties . . . . .	59

## LIST OF FIGURES

Figure 1.1	HAIV concept vehicle . . . . .	2
Figure 1.2	Smoothing criterion . . . . .	4
Figure 1.3	Fragmentation of a kilometer sized asteroid . . . . .	7
Figure 1.4	Subsurface blast through soil . . . . .	8
Figure 1.5	Expanding shockwave traveling through rubble . . . . .	8
Figure 2.1	Tillotson equation of state (Image courtesy of AUTODYN Manual 14.5)	10
Figure 2.2	Simulation setup . . . . .	12
Figure 2.3	Kinetic impact and contact burst . . . . .	12
Figure 2.4	Before and after subsurface explosions . . . . .	13
Figure 2.5	Explosion comparison (100 kT and 250 kT) . . . . .	13
Figure 2.6	Case setup . . . . .	14
Figure 2.7	Case setup . . . . .	15
Figure 2.8	Test point:1a . . . . .	15
Figure 2.9	Test point:2 . . . . .	16
Figure 2.10	Test point:3 . . . . .	16
Figure 2.11	Test point:4 . . . . .	16
Figure 2.12	Test point:5 . . . . .	17
Figure 2.13	Energy transferred to the target . . . . .	17
Figure 2.14	Test point:1b . . . . .	18
Figure 2.15	Test point:6 . . . . .	18
Figure 2.16	Test point:7 . . . . .	18
Figure 2.17	Test point:8 . . . . .	19

Figure 2.18	Case 2 energy transferred . . . . .	19
Figure 2.19	Solver capabilities of AUTODYN . . . . .	21
Figure 2.20	AUTODYN grid representation . . . . .	22
Figure 2.21	Kinetic impact simulation setup . . . . .	23
Figure 2.22	Density and internal energy comparison - kinetic impact . . . . .	23
Figure 3.1	Efficiency plot . . . . .	27
Figure 3.2	JWL equation of state . . . . .	28
Figure 3.3	1D TNT bar geometry and the pressure solutions at 14 microseconds . . . . .	29
Figure 3.4	1D TNT simulation . . . . .	30
Figure 3.5	UNDEX 1D setup . . . . .	31
Figure 3.6	UNDEX 2D axisymmetric Solver . . . . .	32
Figure 3.7	UNDEX 2D planar solver . . . . .	32
Figure 3.8	UNDEX 2D planar solver - pressure solutions . . . . .	33
Figure 3.9	Planar simulation setup . . . . .	33
Figure 3.10	Subsurface (left) and contact (right) simulation pressure solution (JWL) . . . . .	34
Figure 3.11	Subsurface (left) and contact (right) simulation pressure solutions (DED) . . . . .	35
Figure 3.12	2D Axial symmetry (JWL): subsurface (left) and contact(right) pressure solutions . . . . .	36
Figure 3.13	2D Axial symmetry (DED): subsurface (left) and contact (right) pressure solutions . . . . .	37
Figure 4.1	Nodal density (left) and temperature in Kelvin (right) . . . . .	41
Figure 4.2	Sides of the spacecraft . . . . .	42
Figure 4.3	Solid angle calculation . . . . .	42
Figure 4.4	Heat diffusion validation result . . . . .	44
Figure 4.5	Final construction of the algorithm . . . . .	45
Figure 4.6	Thermal test setup and temperature distribution . . . . .	47
Figure 4.7	View factor calculations - side 0 and side 1 . . . . .	47
Figure 4.8	View factor calculations - side 2 . . . . .	48

Figure 4.9	Temperature diffusion - aluminum . . . . .	49
Figure 5.1	Whipple shield setup . . . . .	50
Figure 5.2	BLE curve . . . . .	52
Figure 5.3	Wall thickness comparison . . . . .	53
Figure 5.4	Nodal displacement $75\mu s$ : AUTODYN solution (left) and literature solution (right) . . . . .	54
Figure 5.5	Nodal displacement $500\mu s$ : AUTODYN solution (left) and literature solution (right) . . . . .	55
Figure 5.6	Results - validation 2 . . . . .	56
Figure 5.7	Whipple shield - HAIV . . . . .	57
Figure 6.1	Sod's shock tube solution . . . . .	59
Figure 6.2	Comparison of results - Sod's shock tube . . . . .	60
Figure 6.3	Sedov blast wave - pressure solution . . . . .	61
Figure 6.4	Sedov blast wave . . . . .	62

## ACKNOWLEDGEMENTS

I would like to take this opportunity to express my thanks to those who helped me with various aspects of conducting research and the writing of this thesis. First and foremost, Dr. Bong Wie for his guidance, patience and support throughout this research and the writing of this thesis. I would like to thank Dr. John Basart for his insights and words of encouragement which inspired me and renewed my hopes for completing my graduate education. I would also like to thank Dr. Ganesh Rajagopalan, a great teacher who motivated me to choose a career path in computational fluid dynamics and to become a successful engineer. This research was funded by NASA Innovative Advanced Concepts (NIAC) and Iowa Space Grant Consortium.

## ABSTRACT

Disruption and fragmentation of an asteroid using nuclear explosive devices (NEDs) is a highly complex yet a practical solution to mitigating the impact threat of asteroids with short warning time. A Hypervelocity Asteroid Intercept Vehicle (HAIV) concept, developed at the Asteroid Deflection Research Center (ADRC), consists of a primary vehicle that acts as kinetic impactor and a secondary vehicle that houses NEDs. The kinetic impactor (lead vehicle) strikes the asteroid creating a crater. The secondary vehicle will immediately enter the crater and detonate its nuclear payload creating a blast wave powerful enough to fragment the asteroid. The nuclear subsurface explosion modeling and hydrodynamic simulation has been a challenging research goal that paves the way an array of mission critical information. A mesh-free hydrodynamic simulation method, Smoothed Particle Hydrodynamics (SPH) was utilized to obtain both qualitative and quantitative solutions for explosion efficiency. Commercial fluid dynamics packages such as AUTODYN along with the in-house GPU accelerated SPH algorithms were used to validate and optimize high-energy explosion dynamics for a variety of test cases. Energy coupling from the NED to the target body was also examined to determine the effectiveness of nuclear subsurface explosions. Success of a disruption mission also depends on the survivability of the nuclear payload when the secondary vehicle approaches the newly formed crater at a velocity of 10 km/s or higher. The vehicle may come into contact with debris ejecting the crater which required the conceptual development of a Whipple shield. As the vehicle closes on the crater, its skin may also experience extreme temperatures due to heat radiated from the crater bottom. In order to address this thermal problem, a simple metallic thermal shield design was implemented utilizing a radiative heat transfer algorithm and nodal solutions obtained from hydrodynamic simulations.

## CHAPTER 1. OVERVIEW

HAIV(Hypervelocity Asteroid Impact Vehicle) is a concept vehicle that is being developed at the Asteroid Deflection Research Center (ADRC at Iowa State University). It is designed to address threats from Near Earth Objects (NEO) with relatively short warning times. HAIV blends the energy coupling concepts of kinetic impact and nuclear detonation via a leader-follower spacecraft model. Kinetic impactor, the leading vehicle houses guidance and navigation equipment. The impactor crashes into the asteroid creating a crater. The secondary vehicle which carries the Nuclear Explosive Device (NED) enters the crater and couples energy to the asteroid via a blast wave. The amount of energy coupled determines the quantity and the mode of fragmentation [4, 5]. The Magnitude of energy coupling, asteroid material parameters and the asteroid geometry determines the mass of the fragments which may enter into a collision trajectory with the earth. Therefore, optimizing the nuclear explosion plays a key role in minimizing the mass of the fragments.

Protecting the secondary vehicle from the excessive heat of the crater created by the initial impact and fast moving ejecta also presents a challenge that will be addressed with the design of thermal and Whipple Shields.

### 1.1 Introduction

Simulating a hyper-velocity impact and the nuclear explosion via a computational fluid dynamics approach leads to accurate predictions which will be used to design thermal and Whipple shields and to optimize the fragmentation.

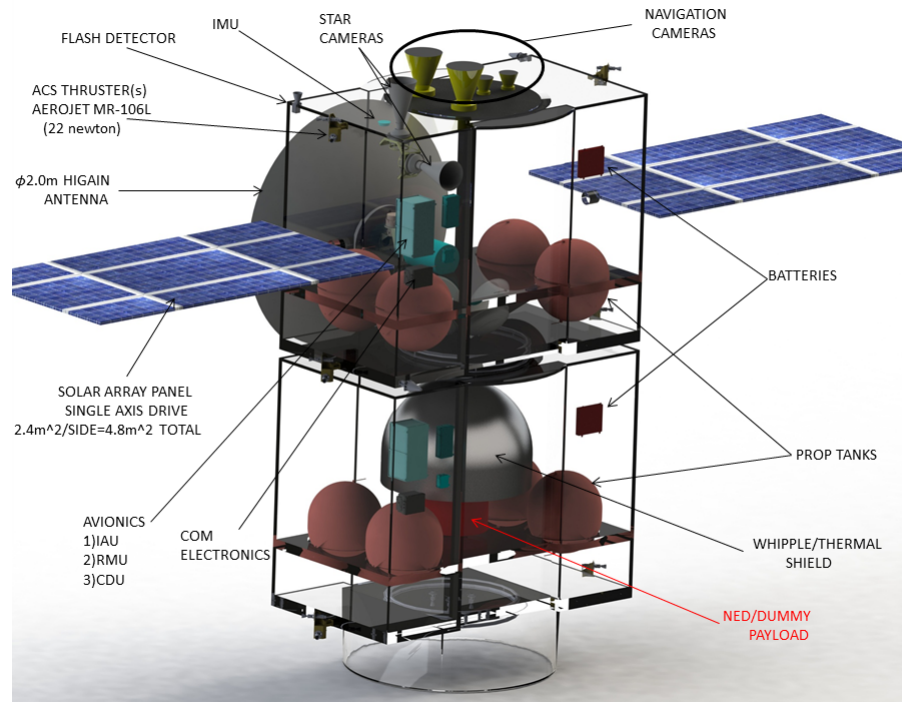


Figure 1.1 HAIV concept vehicle

Smoothed Particle Hydrodynamics (SPH), a mesh less particle physics method was utilized to simulate hypervelocity impacts and a subsurface nuclear detonation for a given target. A GPU accelerated SPH algorithm developed by Dr. Brian Kaplinger was initially used to obtain qualitative solutions for the HAIV approach. This algorithm provided high resolution solutions for a variety of simulation scenarios including subsurface explosions, contact explosions and integrated HAIV approaches. A commercial algorithm, AUTODYN, developed by ANSYS, Inc was used to extend the simulation work done in the past by obtaining validated qualitative and quantitative solutions related to shock propagation, fragmentation and energy coupling.

## 1.2 SPH method

The SPH method is a Lagrangian particle physics method, initially used to perform cosmological simulations [1]. It is formulated with the basic fluid dynamic equations smoothed over a kernel function  $W$  for a calculated or specified smoothing length. The kernel function, usually specified as a cubic spline, modifies the basic fluid dynamic equations via averaging to obtain

the following conservation of mass, momentum, and energy equations [1].

### 1.2.1 Formulation

The formulation of the SPH method is based on the basic equations of fluid dynamics written in a Lagrangian system. The substantial derivatives consists of conservation of mass, momentum and energy are denoted by

$$\begin{aligned}
 \frac{D\mathbf{x}_i}{Dt} &= \mathbf{v}_i \\
 \frac{D\rho_i}{Dt} &= \sum_{j=1}^N m_j (\mathbf{v}_i - \mathbf{v}_j) \cdot \nabla_i W_{ij} \\
 \frac{D\mathbf{v}_i}{Dt} &= \sum_{j=1}^N m_j \left( \frac{p_i}{\rho_i^2} + \frac{p_j}{\rho_j^2} + \mu_{ij} \right) \nabla_i W_{ij} \\
 \frac{De_i}{Dt} &= \frac{1}{2} \sum_{j=1}^N m_j \left( \frac{p_i}{\rho_i^2} + \frac{p_j}{\rho_j^2} + \mu_{ij} \right) (\mathbf{v}_i - \mathbf{v}_j) \cdot \nabla_i W_{ij}
 \end{aligned} \tag{1.1}$$

where properties of the  $i^{th}$  particle depend on the properties of an aggregate of N number of neighbor particles. Substantial time derivatives of density( $\rho$ ), internal energy( $e$ ), and velocity( $v$ ) are solved by an explicit time integration scheme such as Runge Kutta or leap frog integration. Pressure ( $p$ ) is calculated by an equation of state which represents material properties of each node. The SPH method is considered an ideal multi-material solver where the user is able to specify material interactions and complex phase changes. Nodal mass of a neighbor particle is given as  $m_j$ . Density, velocity and specific internal energy for a given particle are smoothed over a changing smoothing length ( $h$ ) using a cubic spline kernel function ( $W_{ij}$ ). An artificial viscosity term ( $\mu_{ij}$ ) for efficient shock capturing is also introduced. This term will be described in detail later on.

### 1.2.2 Kernel Function

The kernel function ( $W$ ) plays a major role in determining properties of a particle. A cubic spline is widely used in SPH formulations. Cubic spline equations can be easily changed in a SPH algorithm to cater for different type of simulations. The kernel function is defined by

$$W = \frac{\sigma}{h^\nu} \begin{cases} 1 - \frac{3}{2}q^2 + \frac{3}{4}q^3 & 0 < \frac{r}{h} < 1 \\ 1 - \frac{1}{4}(2 - q^3) & 1 < \frac{r}{h} < 2 \\ 0 & r > 2h \end{cases} \quad (1.2)$$

where  $r$  is defined as the magnitude of displacement between  $i$ th and  $j$ th particle and  $q$  is  $\frac{r}{h}$ . If the radius length surpasses twice the smoothing length, neighbor particles beyond  $2h$  will not be used to calculate the gradient vector of  $W$ . The factor  $\frac{\sigma}{h^\nu}$  is dependent on the number of dimensions where the dimension is denoted by  $\nu$ .

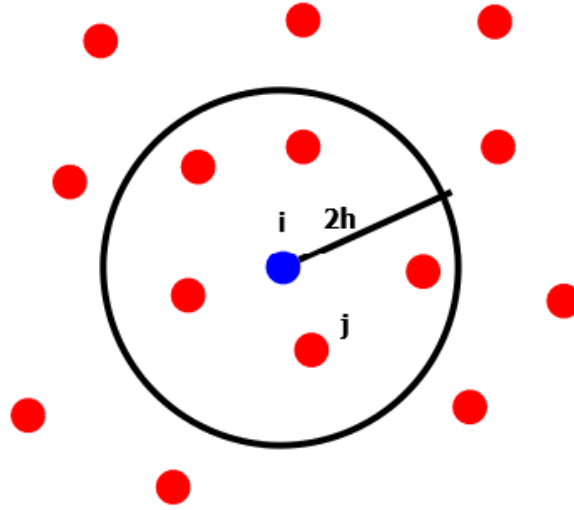


Figure 1.2 Smoothing criterion

A smoothing criterion for the  $i^{th}$  particle is shown in Figure 1.2. Smoothing length can also be subjected to a time dependent change for a better accuracy. The substantial derivative of the smoothing length is given by

$$\frac{Dh_i^n}{Dt} = -\frac{h_i^n}{\rho_i^n d} \frac{D\rho_i^n}{Dt} \quad (1.3)$$

where  $d$  is the number of dimensions and  $\rho_i^n$  and  $h_i^n$  are defined as density and smoothing length of the  $i^{th}$  particle at the  $n^{th}$  time step. The smoothing length at the  $n^{th}$  time step can be calculated by using an explicit scheme.

$$h_i^{n+1} = h_i^n + \frac{Dh_i^n}{Dt} \Delta t \quad (1.4)$$

A relaxation factor  $\theta$  can be introduced to this equation for an optimized answer, especially for large deformation simulations (e.g., explosions),

$$h_i^{n+1} = h_i^n + \theta \frac{Dh_i^n}{Dt} \Delta t \quad (1.5)$$

A fixed or variable  $h$  scheme can be implemented in AUTODYN through the solver options.

### 1.2.3 Artificial Viscosity

Artificial viscosity term ( $\mu_{ij}$ ) is implemented in hydrodynamic simulations to model shock waves without unphysical oscillations. Monaghan type artificial viscosity terms are popular in SPH literature as they prevent unphysical particle penetration at the material interfaces and capture the shocks without numerical artifacts, as

$$\mu_{ij} = \begin{cases} \frac{-\alpha c_{ij} \phi_{ij} + \beta \phi_{ij}^2}{\rho_{ij}} & \mathbf{v}_{ij} \cdot \mathbf{x}_{ij} < 0 \\ 0 & \mathbf{v}_{ij} \cdot \mathbf{x}_{ij} \geq 0 \end{cases} \quad (1.6)$$

where,

$$\begin{aligned} \phi_{ij} &= \frac{h_{ij} \mathbf{v}_{ij} \cdot \mathbf{x}_{ij}}{|\mathbf{x}_{ij}|^2 + \varphi^2} \\ c_{ij} &= \frac{1}{2}(c_i + c_j) \\ \rho_{ij} &= \frac{1}{2}(\rho_i + \rho_j) \\ h_{ij} &= \frac{1}{2}(h_i + h_j) \\ v_{ij} &= \mathbf{v}_i - \mathbf{v}_j \end{aligned} \quad (1.7)$$

Subscript  $ij$  denotes a change in vector or scalar property between the  $i^{th}$  particle and its  $j^{th}$  neighbor particle. Linear and quadratic viscosities ( $\alpha, \beta$ ) are set to 1.0 for many simulations

but they should be altered depending on the type of simulation. Speed of the sound in  $i^{th}$  node is given by  $c_i$ .

### 1.2.4 Time Integration

An adaptive time scheme also increases the stability of a SPH algorithm. A Courant-Friedrichs-Levy (CFL) condition is introduced to adjust the time step proportional to the smoothing lengths.  $dt$  is calculated for each particle using

$$\Delta t = \min\left(\frac{\xi h_i}{h_i \nabla \cdot \mathbf{v}_i + 1.2(\alpha c_i + \beta h_i |\nabla \cdot \mathbf{v}_i|)}\right) \quad (1.8)$$

and the minimum time step is selected for the next iteration. The Courant number ( $\xi$ ) is kept at 0.3 during many types of simulations.  $\alpha$  and  $\beta$  values used in calculating artificial viscosity are also used in this equation. Both AUTODYN and in-house GPU algorithms allow the user to manually decrease the time step in the presence of an instability.

A sample leap-frog integration is normally used to advance the properties of each particle as suggested in the equations below [7]:

$$\begin{aligned} t &= t + \Delta t \\ \rho_i(t + \Delta t/2) &= \rho_i(t - \Delta t/2) + \Delta t \cdot D\rho_i(t) \\ v_i(t + \Delta t/2) &= v_i(t - \Delta t/2) + \Delta t \cdot Dv_i(t) \\ u_i(t + \Delta t/2) &= u_i(t - \Delta t/2) + \Delta t \cdot Du_i(t) \\ x_i(t + \Delta t) &= x_i(t) + \Delta t \cdot v_i(t + \Delta t/2) \end{aligned} \quad (1.9)$$

The explicit scheme implemented that reduces the computational time as a matrix solver is not needed. However, the explicit scheme may cause instabilities for high resolution grids.

### 1.3 History of Hydrodynamic Modeling

The SPH method was initially developed by Gingold, Monaghan and Lucy to solve large scale astrophysical problems (e.g., galaxy formations). Introduction of this method presented a robust platform for many high energy scenarios. The need for a grid was eliminated in this method as geometries were represented using a nodal/particle distribution, thus eliminating issues such as grid collapsing [1]. The SPH method also conserves energy, continuity and momentum with low error percentages compared to traditional grid-based methods. A zero dissipation in state properties in the method allows users to extract time sensitive information such as shock pressure magnitudes without under predictions.

Due to these qualities, SPH has been re-invented as a simulation method for a wide variety of fragmentation and explosion problems. In order to simulate varying material phases and types, the SPH method was coupled with different equations of state and material strength models. Therefore, the SPH method was introduced as a viable option in performing hypervelocity impacts in asteroids. Various fragmentation models have been used with induced cracks in the asteroid geometry to model material failure and disintegration of the celestial body as shown in Figure 1.3 [28].

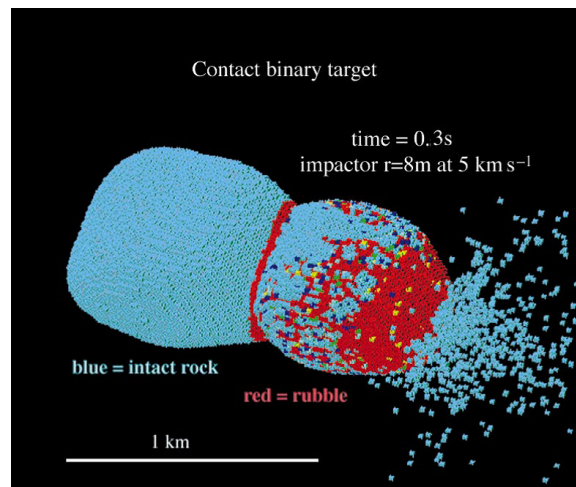


Figure 1.3 Fragmentation of a kilometer sized asteroid

The SPH method is also being used as a method to model blast waves due to conventional explosive payloads. With the recent developments in commercial algorithms, users are able to

utilize accurate explosion models and other material models. The SPH method may also get coupled with a finite element model to measure structural deformations. The results obtained in these simulations are often compared with known shock wave data. A sample subsurface blast inside soil is shown in Figure 1.4. This data was later expanded to model deformation of a concrete structure [24].

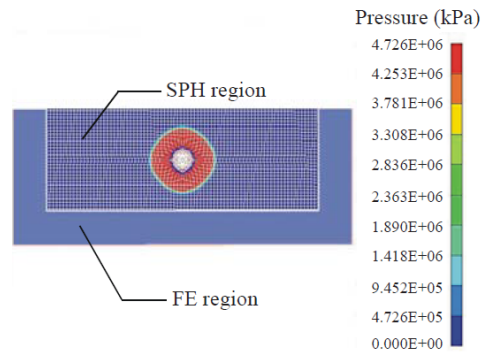


Figure 1.4 Subsurface blast through soil

Such research provided necessary motivation and inspiration for the initial SPH simulations done at ADRC. A GPU accelerated algorithm was developed which incorporated a material fragmentation model. A Weibull distribution was used to create implicit flaws in a given asteroid geometry. A basic blast model was also integrated that sources energy into a pre-defined set of particles governed by Tillotson equation of state. A sample simulation of a shock wave traveling through rubble like asteroid geometry is shown in Figure 1.5 [23].

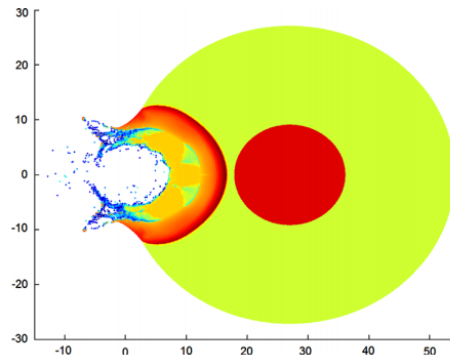


Figure 1.5 Expanding shockwave traveling through rubble

## CHAPTER 2. Simulation Capabilities

This chapter discusses material modeling, grid generation and initial simulations using both in-house algorithm and AUTODYN. Most of the initial simulations were conducted to obtain qualitative solutions for energy coupling methods of the HAIV concept vehicle (ie: hyper-velocity impact, explosion simulations) using the in-house algorithm. A series of sensitivity studies were done to demonstrate the use of an in-house algorithm in determining the guidance requirements for the secondary vehicle (NED). A simple comparison between the in-house algorithm and AUTODYN is also presented in this chapter.

### 2.1 Material Modeling

Material modeling of asteroids has been an extremely complicated challenge. Asteroids consist of materials ranging from metals to gaseous compounds arranged in heterogeneous distributions. Structural integrity of an asteroid is also considered as a hard to predict input argument in a simulation environment as it may range from a solid to a shattered rubble pile held together by gravity. As most of the previous simulation work was done assuming homogeneous density layers, research described in this thesis was also conducted with that assumption. Initial material modeling was done using the Tillotson equation of state. A failure criterion based on Weibull distribution was introduced to initialize pre-shattered geometries. The Tillotson equation of state predicts metallic material behavior during energy transfer modes. This equation defines material phase changes, compressions, and expansions based on energy transfer. The Tillotson equation of state is defined for four regions located to the right of the Hugoniot curve. Figure 2.1 depicts the four regions that define shock compression [2].

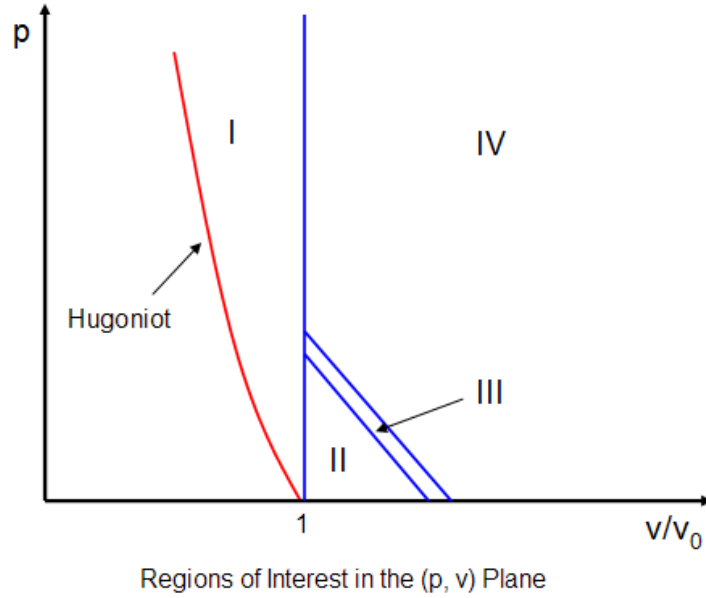


Figure 2.1 Tillotson equation of state (Image courtesy of AUTODYN Manual 14.5)

Within region I, the material is represented in a compressed state. The vertical line extends up to 1000 Mbar and the pressure is given as

$$P_1 = \left(a + \frac{b}{\omega_0}\right)\eta\rho_0 E + A\mu + B\mu^2 \quad (2.1)$$

Region II defines material characteristics under shock due to energy that is less than the sublimation energy. The pressure here is

$$P_2 = \left(a + \frac{b}{\omega_0}\right)\eta\rho_0 E + A\mu \quad (2.2)$$

At region III, the pressure is just the mean pressure between regions II and IV given by

$$P_3 = P_2 + \frac{(P_4 - P_2)(E - E_s)}{E'_s - E_s} \quad (2.3)$$

The expansion phase of a shocked material is governed by Region IV with pressure defined as

$$P_4 = a\eta\rho_0 E + \left(\frac{b\eta\rho_0 E}{\omega_0} + A\mu e^{\beta x}\right) e^{-\alpha x^2} \quad (2.4)$$

where  $x = 1 - \frac{1}{\eta}$ . Material parameters, such as  $a$ ,  $b$ ,  $\alpha$  and  $\beta$ , are fitting parameters for the Tillotson equation of state. The parameter  $A$  is considered the bulk modulus and  $B$  represents

the compressive term. Parameters such as  $\omega_0$ ,  $\eta$  and  $\mu$  are defined by:

$$\begin{aligned}\eta &= \frac{\rho}{\rho_0} \\ \mu &= \eta - 1 \\ \omega_0 &= 1 + \frac{E}{E_0\eta^2}\end{aligned}\tag{2.5}$$

where the reference or initial values are denoted by subscript “0”. The specific internal energy ( $E$ ) and the density ( $\rho$ ) play a major role in determining the phase and pressure of the metallic material. Sublimation energy of the material is given by  $E_s$  while the  $E'_s$  represents the energy required for the material to expand as a gas. This parameter is combination of sublimation energy and a fraction of vaporization energy.

A Tillotson material model is an efficient method of modeling pre-shattered rubble piles. A linear relationship between a shock wave and particle velocities lays the foundation for this equation of state and it has provided results that agrees with laboratory experiments. This model was used to represent the particle distribution of the target asteroid in blast simulations and hypervelocity impacts. The same model was also employed in designing a basic Whipple shield discussed in Chapter 5.

## 2.2 HAIV concept simulation

A batch of simulations was initially constructed to demonstrate and understand the in-house SPH algorithm and its capabilities. A comparison between AUTODYN and the in-house algorithm is also included in this chapter.

Initial simulations were conducted to demonstrate the following scenarios which are vital to HAIV mission design.

1. **Kinetic impact** : A pure kinetic impact without the nuclear payload.
2. **Contact Burst** : The payload explodes upon contact with the asteroid
3. **Subsurface explosion** : The nuclear payload was detonated after it partially/fully submerges inside the specified target.

4. A comparison between a 100 kt and a 250 kt war head detonation in order to observe qualitative trends of the explosion. (ex: A higher compression and particle dispersion was expected from the detonation of 250 kT war head compared to 100kT)

In order to simulate this scenario, a target with a solid granite core and a rubble outer crust was introduced [23]. A simulation setup is shown in Figure 2.2.

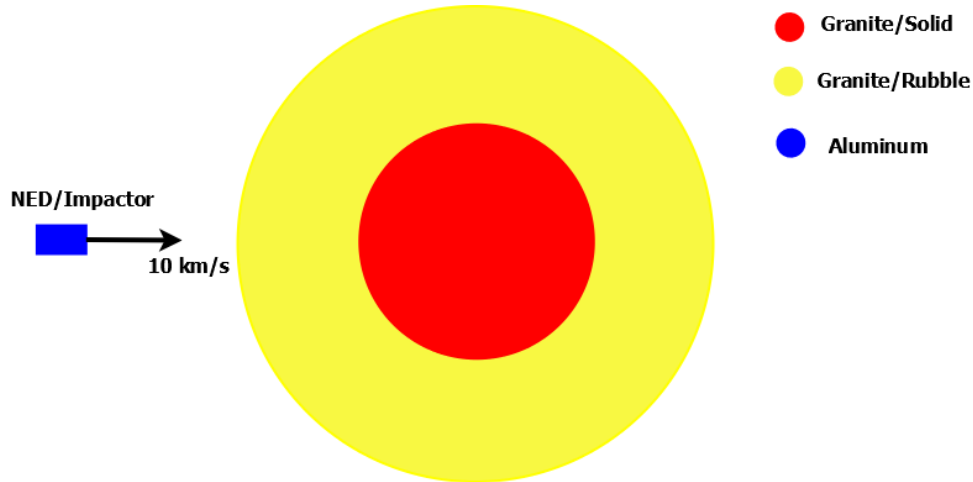


Figure 2.2 Simulation setup

Simulations were run until a clear shock propagation can be observed. Results for the above mentioned scenarios are provided in Figure 2.3, Figure 2.4 and Figure 2.5.

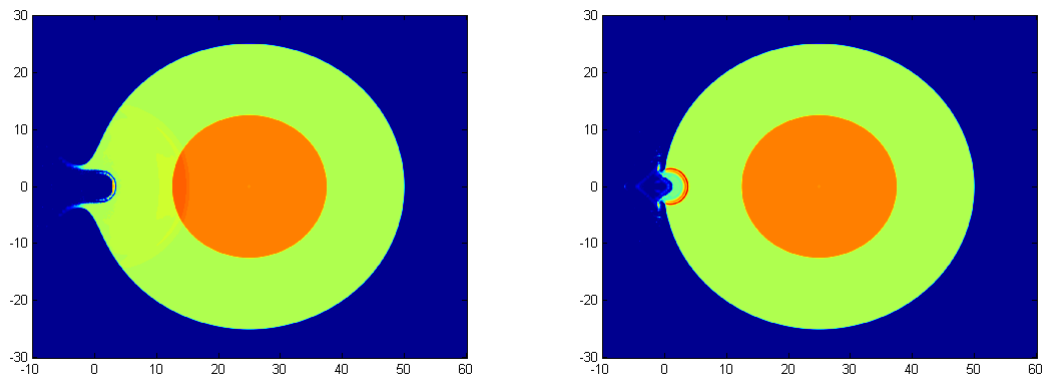


Figure 2.3 Kinetic impact and contact burst

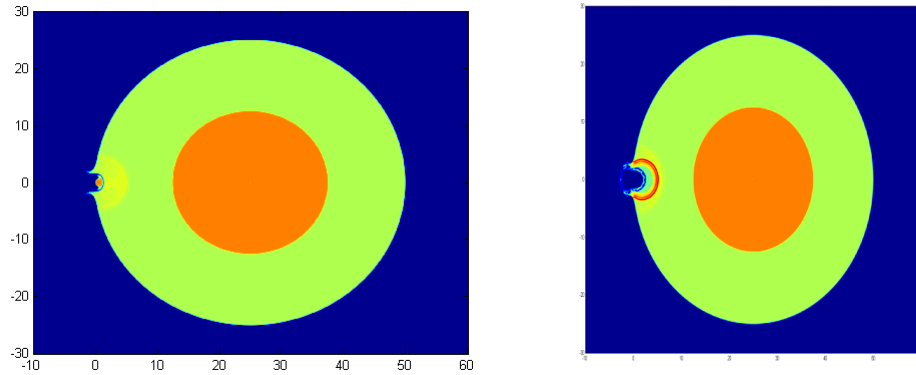


Figure 2.4 Before and after subsurface explosions

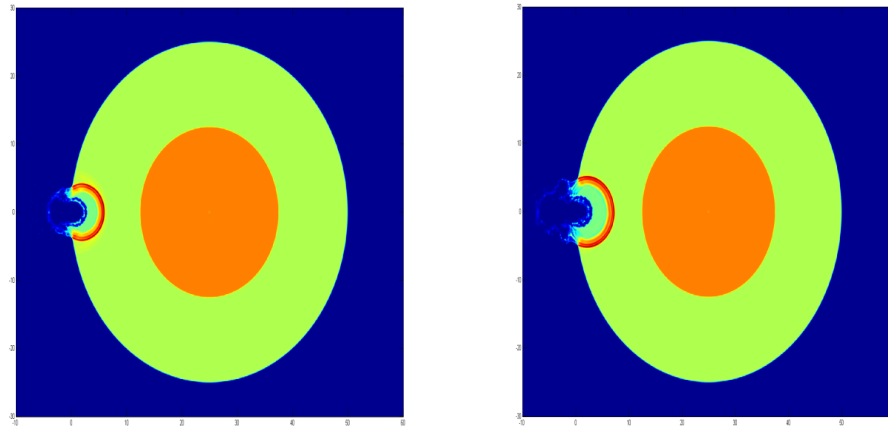


Figure 2.5 Explosion comparison (100 kT and 250 kT)

A bow shock propagation was detected after the NED was triggered. The shock magnitude seems to be a lot higher in the explosion scenarios compared to the pure kinetic impact. Particle dispersion due to the initial impact occurs tangent to the crater boundary. As depicted in Figure 2.5, the 250 kt explosion depicts a shock front larger in magnitude compared to the one generated by the 100 kt explosion. Therefore, qualitative results obtained in the simulation agrees with the expected trends of bow shock propagations and particle dispersion.

### 2.3 Sensitivity Studies

A series of sensitivity and validation studies using a 2D SPH (Smooth Particle Hydrodynamics) algorithm were conducted in order to identify mission critical information. The tests incorporated a spacecraft model with a leading impactor and a following nuclear payload. A 70 m wide asteroid was set as the target and the studies below were performed to determine a location to detonate the payload which optimizes fragmentation [6]. Total energy coupled to the asteroid was recorded for both cases in order to quantify the damage.

1. **Case 1 :** Once the impactor creates a crater, the payload was guided to different locations of the crater to identify the magnitude of the damage caused by each nuclear detonation scenario.
2. **Case 2 :** The NED was detonated in a series of locations above and below the surface level of the crater created by initial impact. Density distributions were obtained to observe damage done to the asteroid.

The detonation locations for each case are shown in Figure 2.6.

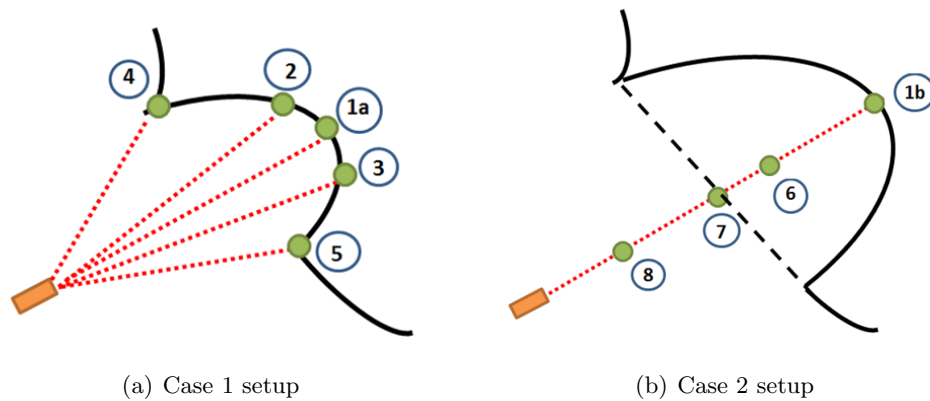


Figure 2.6 Case setup

A grid representation of the asteroid body, kinetic impact and the follower vehicle is illustrated in Figure 2.7. A zoomed view of the vehicle setup is also shown next to the grid setup in Figure 2.7(b). The triangular particle distribution represents the kinetic impactor while the

rectangular particle distribution depicts the NED. The grid consisted more than 800,000 nodes with the outer layers constructed out of rubble with a solid core.

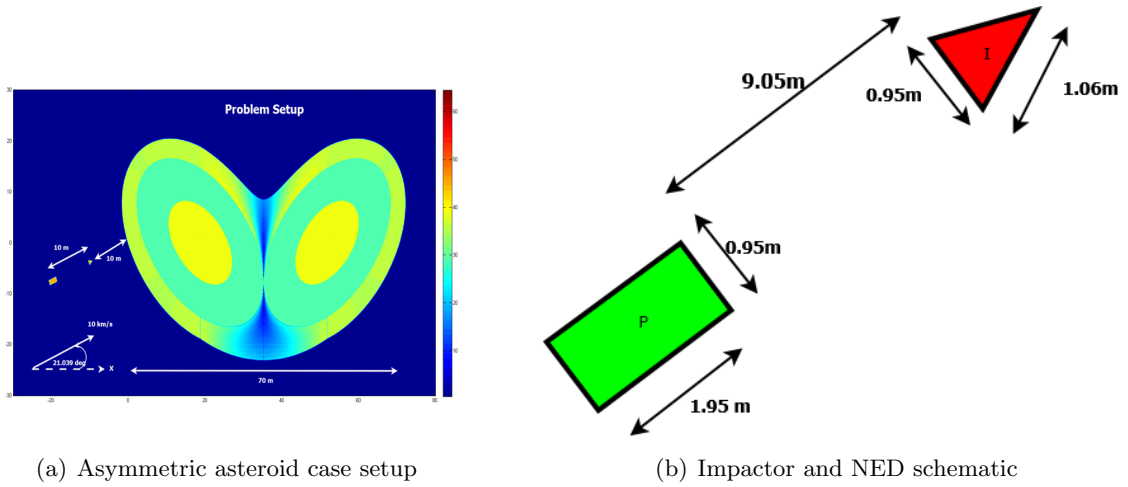


Figure 2.7 Case setup

### 2.3.0.1 Case 1 Results

Qualitative results for the problem are given in Figure 2.8 to Figure 2.12. They show density solutions, before and after the nuclear detonations.

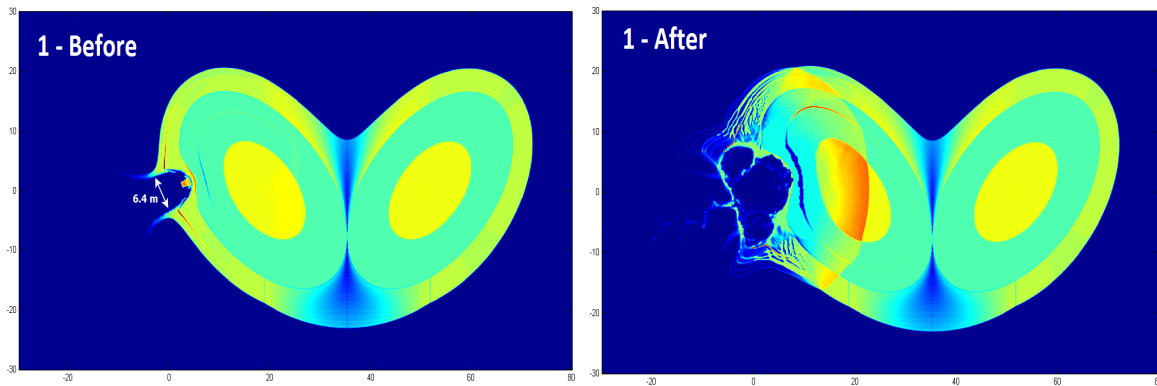


Figure 2.8 Test point:1a

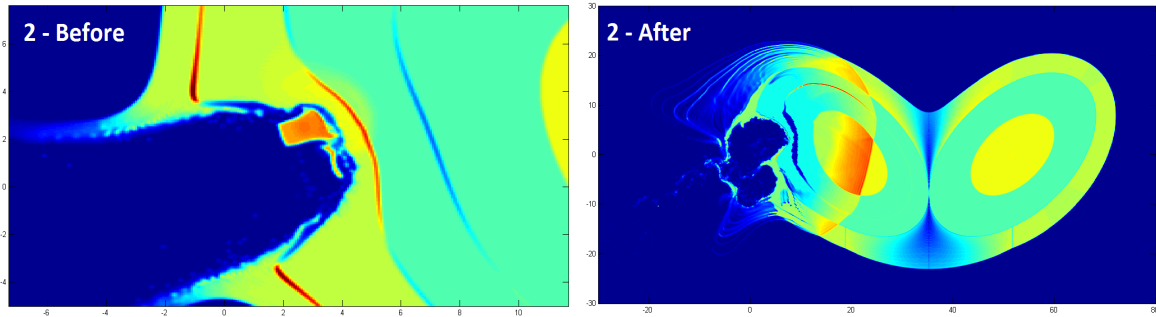


Figure 2.9 Test point:2

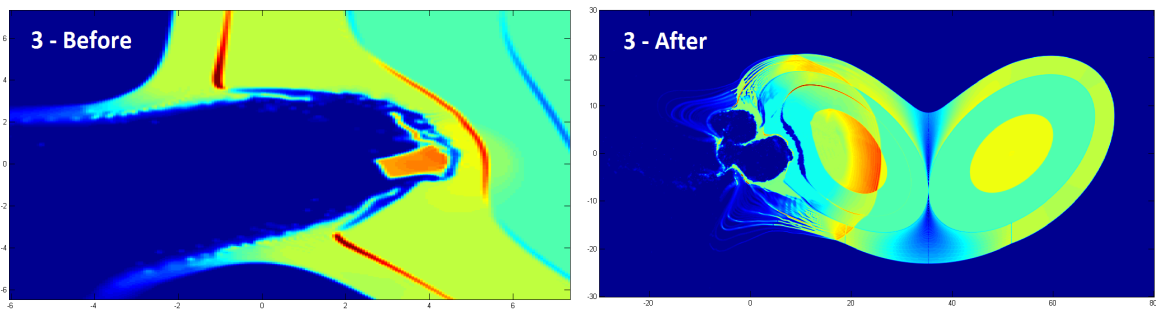


Figure 2.10 Test point:3

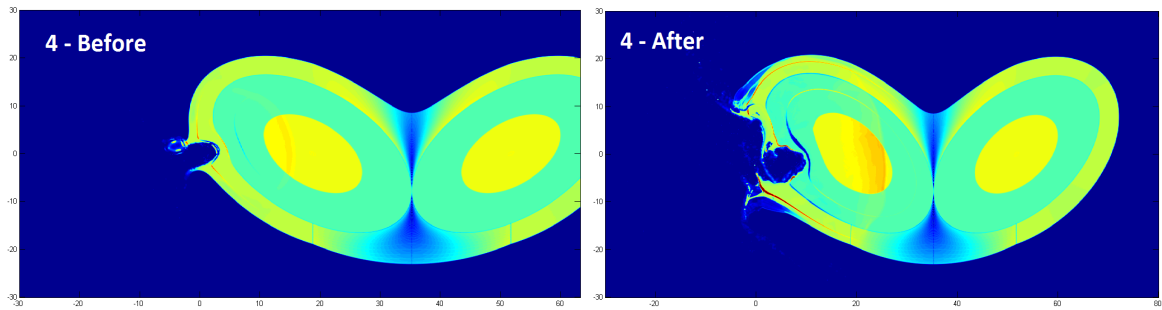


Figure 2.11 Test point:4

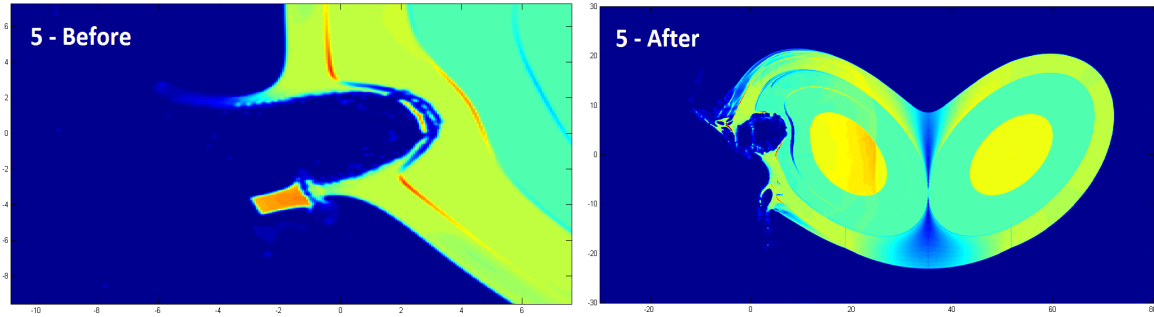


Figure 2.12 Test point:5

Total energy coupled to the target body was plotted along the location number as shown in Figure 2.13. This information paves the way for designing an efficient steering mechanism for the secondary vehicle.

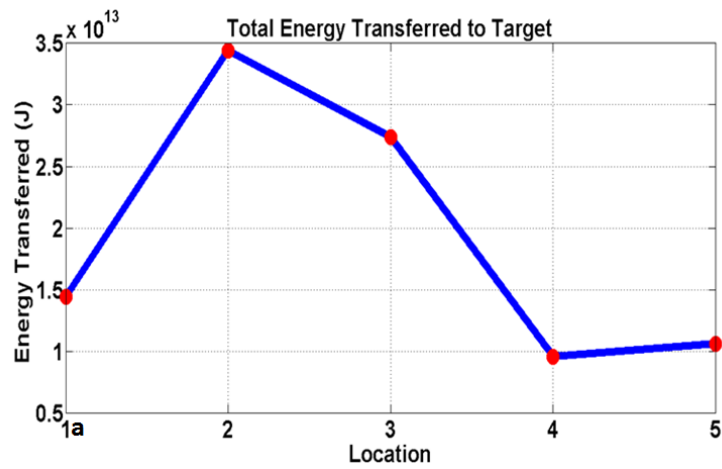


Figure 2.13 Energy transferred to the target

### 2.3.0.2 Results Case 2

Qualitative density distributions before and after the detonation of NED at each position are shown from Figure 2.14 to Figure 2.17.

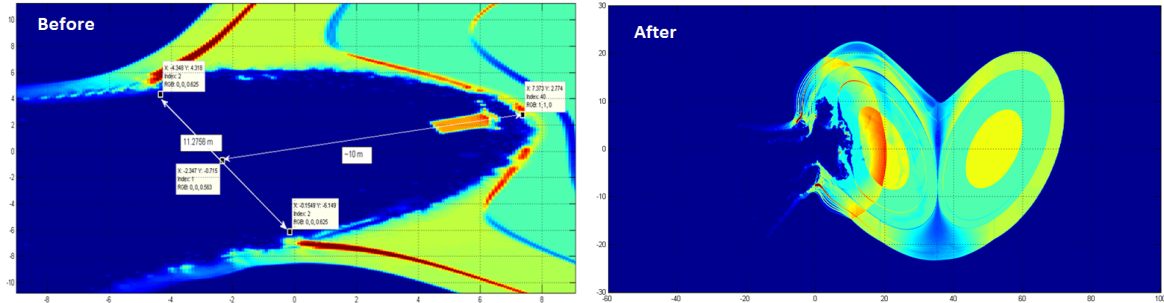


Figure 2.14 Test point:1b

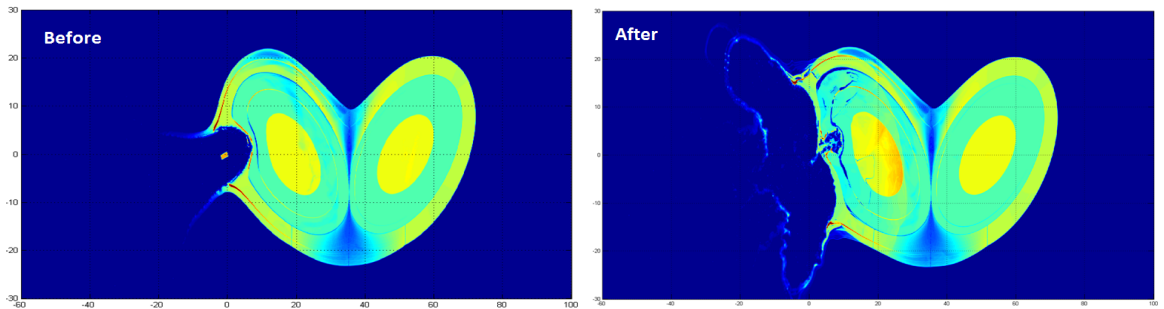


Figure 2.15 Test point:6

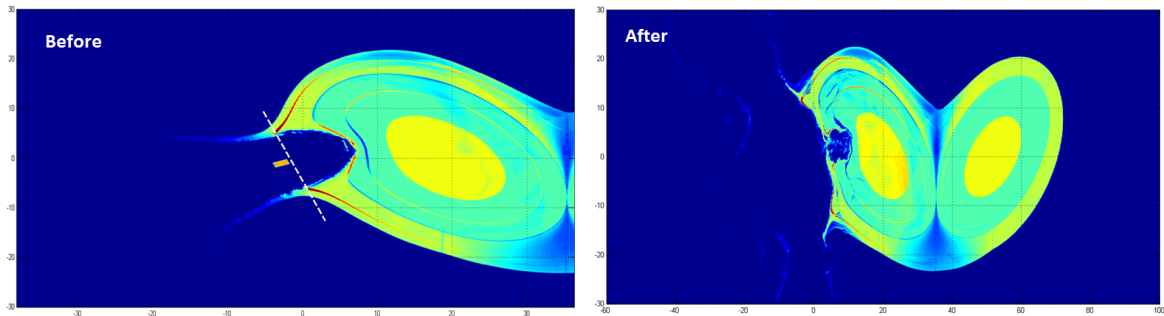


Figure 2.16 Test point:7

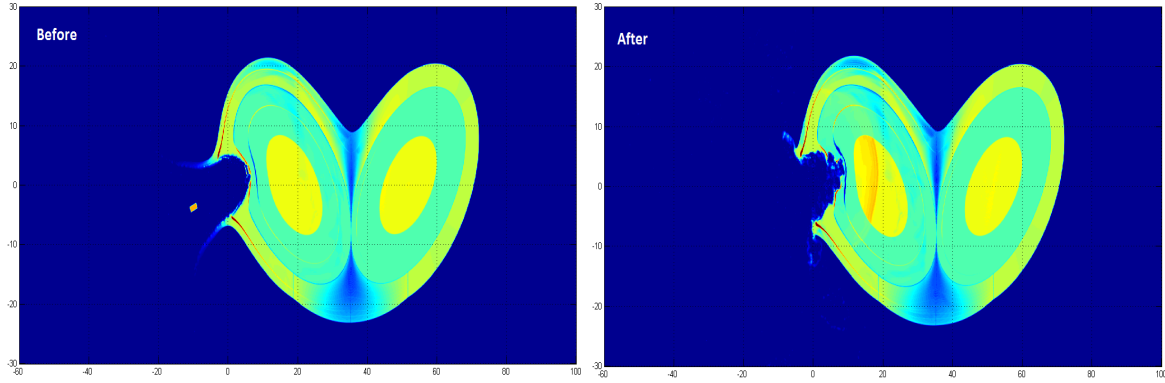


Figure 2.17 Test point:8

Total energy transferred to the asteroid via the detonation is shown in Figure 2.18 along with the stations on line of sight. This graph can be utilized in a real scenario to predict where the device should be detonated in case reaching the bottom of the crater is not a viable option.

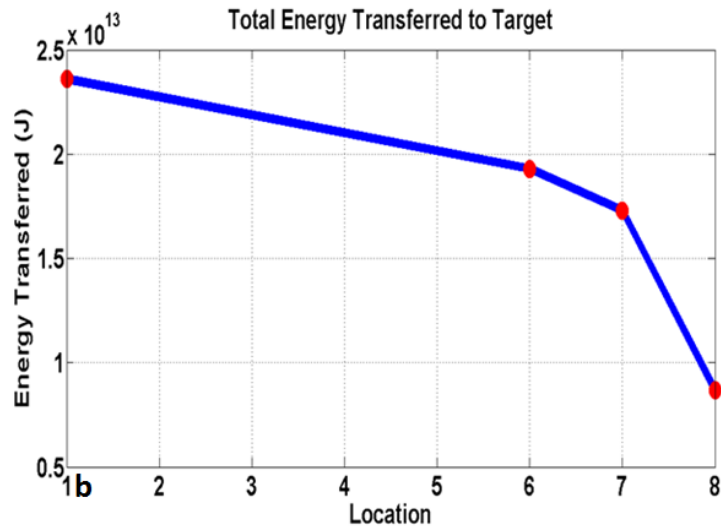


Figure 2.18 Case 2 energy transferred

### 2.3.0.3 Analysis

- **Case 1:** Detonating the payload in Location 2 caused the maximum damage to the asteroid. It clearly shows a much larger energy coupling compared to other scenarios. Location 2 and 3 show qualitative solutions comprising of bow shock propagations towards the core. Location 4 and 5 also shows some symmetry of the solutions when compared. However, those locations don't seem to be efficient in fragmenting the asteroid and inflicting significant damage to the asteroid as seen in location 2 and location 3. The void created by the initial impact moved upwards and downwards due to the force exerted on the asteroid particles by the nuclear detonation. The energy coupling to the asteroid is maximum at location 2 due to the asymmetric nature and the heterogeneous material distribution of the geometry.
- **Case 2 :** When the location of the nuclear explosion moves away from the bottom of the crater, the damage inflicted on the asteroid seems to be becoming less due to low amounts of energy coupling. This could be due to high energy particles resulting from the blast moving in many directions. Some of these particles may not come in to direct contact with the asteroid at all.

## 2.4 AUTODYN vs In House Algorithm

### 2.4.1 AUTODYN

AUTODYN by ANSYS, Inc is an explicit algorithm used in many engineering disciplines to simulate hypervelocity impacts, explosions and other multi-material interactions. The software comes with a wide variety of simulation methods ranging from grid based Eulerian fluid simulations to the Lagrangian SPH method described in Chapter 1. A user friendly GUI environment, complete with a visualizer allow researchers to monitor and post-process solutions efficiently [2].

## 2.4.2 Solver Capabilities

A complete evaluation of AUTODYN's capabilities was performed in order to identify potential simulation methodologies for a Whipple shield design. The 2D simulations have been utilized as a computationally inexpensive and an efficient method to model multi-physics scenarios. The complete capability list found is given in Figure 2.19.

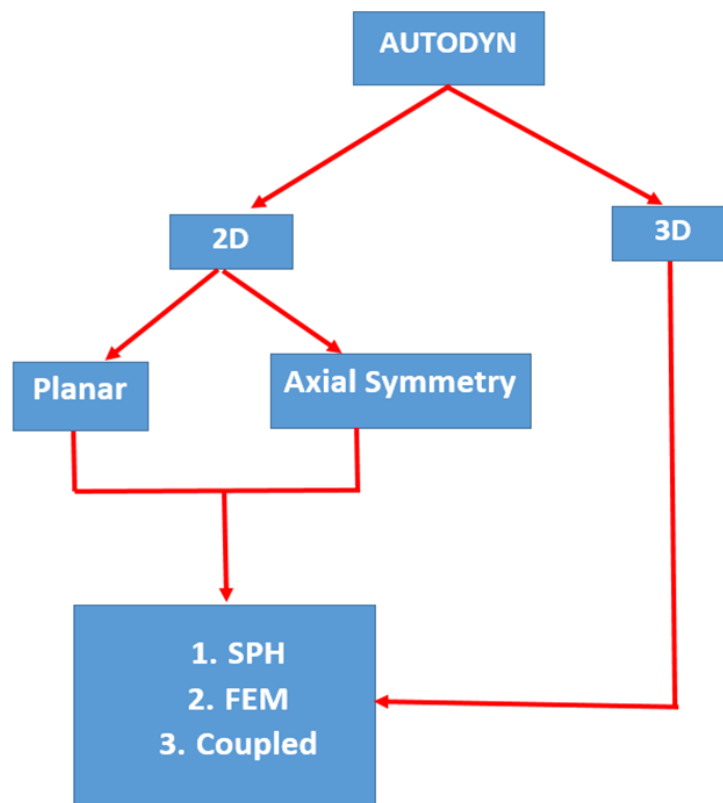


Figure 2.19 Solver capabilities of AUTODYN

In addition to these capabilities Workbench also provides a CAD module similar to solid works and a Mechanical editor that allows the user to utilize the AUTODYN solver for simulations without having to use the AUTODYN GUI. Eulerian simulation options are also available and coupled with a Lagrangian framework with the help of ALE (Arbitrary Lagrangian Eulerian). An Eulerian grid can be used to simulate explosions, fluid flow over bodies etc and provides a stable simulation platform for air-based simulations governed by the ideal gas law.

The SPH method available through AUTODYN is currently incapable of handling compressible fluid flow governed by ideal gas law [8].

- **Planar Modeling:**

A 2D simulation with a planar model suggests the strain in the z direction is zero (plain strain approach). The model can be considered as the cross section of a 3D model elongated along the z axis. The in house SPH algorithm was developed as a planar simulation platform. Results produced in this framework is analogous to a cylindrical 3D environment.

- **Axisymmetric Modeling :** An axisymmetric simulation can be performed for cases that involved simple geometries that are symmetric over an axis line (X, Y and Z). The user is only required to create half of the Eulerian or Lagrangian grid where it will be rotated around an axis of symmetry. After a solution has been obtained, the 2D solution can be rotated around the axis to obtain a corresponding 3D solution. Axisymmetric simulations can reduce the simulation time and the set up time for a case and while producing results analogous to an actual 3D case. However, this method will not do any justice for cases with oblique geometries and asymmetrical scenarios (ex: hypervelocity impacts at an angle). A grid representation for both types is given in Figure 2.20.

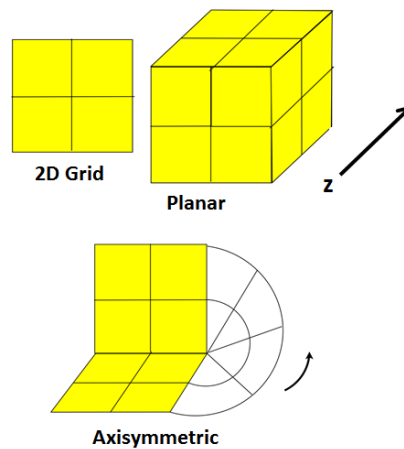


Figure 2.20 AUTODYN grid representation

### 2.4.3 SPH Solver Comparison

In order to compare the solvers of both in-house and AUTODYN, a hypervelocity impact case was setup with similar grid resolution. The planar SPH solver was used for this purpose with the material properties were governed by Tillotson equation of state. A sample setup is shown in Figure 2.21.

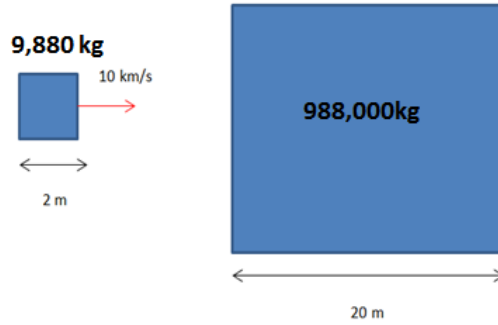


Figure 2.21 Kinetic impact simulation setup

The density and specific internal energy solutions from both simulations are compared in the Figure 2.22.

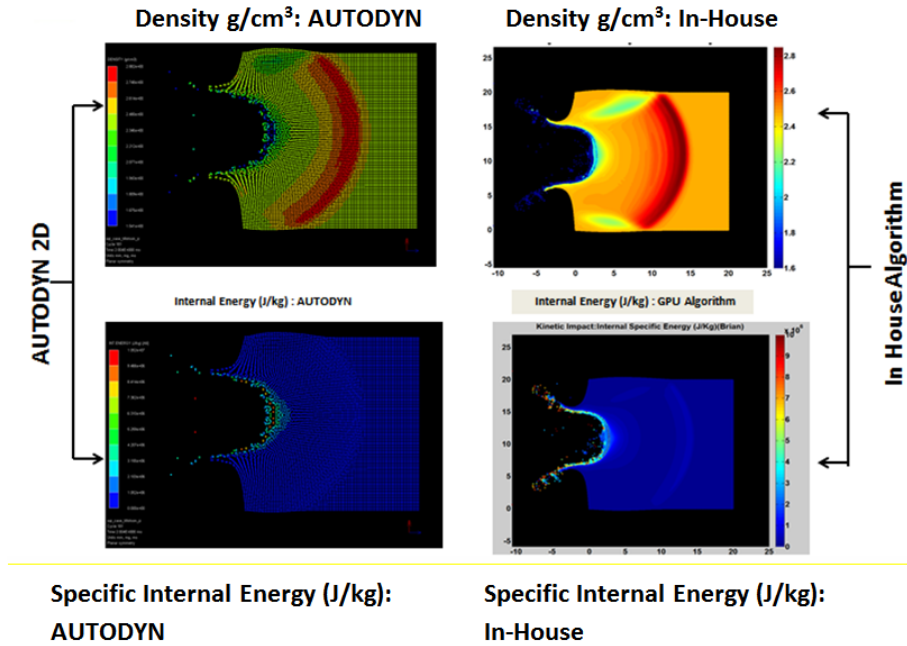


Figure 2.22 Density and internal energy comparison - kinetic impact

A bow shock propagation due to the impact can be seen in both solutions along with a crater formation. As the shock wave approaches the outer border it starts deforming. Crater depth was measured to be 6.0 m while the width was approximately 10 m. However, the in house algorithm over-predicted the internal energy calculations. Significant non-physical artifacts also started appearing in high energy simulations such as the sub-surface explosions. Solutions seems to be diverging and the symmetry was not maintained. Therefore, the future simulations related to blast optimization were conducted using AUTODYN.

## CHAPTER 3. Blast Simulation and Modeling

Optimizing the blast created from the nuclear explosive device plays a predominant role in fragmenting the asteroid. This chapter discusses blast simulation techniques developed at the ADRC to simulate energy coupling and the corresponding fragmentation of the asteroid. Initial simulations were conducted as high density gas explosions utilizing conventional explosives such as TNT. Nuclear blast modeling presented a far greater challenge as the vast quantities of internal energy resulted in unstable simulations. The experimental data sets and modeling techniques for nuclear blast waves were recorded in classified material thus creating an obstacle in validating and designing algorithms. The SPH method was used to simulate blast scenarios due to its stable nature in high deformation problems. However, the Eulerian multi-material solver has been utilized in the recent simulations as the SPH method failed to show stability during air blasts.

### 3.1 Initial Settings

This section discusses the modeling of hydrodynamic simulations via the SPH method. The data for material models was extracted from previous works of literature in the field and documentation provided by ANSYS. The explosive device chosen in most simulations is Trinitrotoluene (TNT). Energy coupling is modeled via two methods: Direct energy deposition and Jones-Wilkins-Lee (JWL) equation of state. The direct energy deposition model was initially used in the in-house GPU SPH algorithm and was implemented in AUTODYN for comparison. The CPR method, a higher order grid based algorithm under development, currently uses only the direct energy deposition model for simulations [25].

### 3.1.1 Energy Coupling Methods

A series of studies are currently underway to investigate the energy coupling by the explosive to the asteroid. The energy deposition schemes below are tested and employed for a wide variety of 2D and 3D SPH simulations presented in this chapter [25].

- **Direct Energy Deposition (DED):** Upon specifying a yield for the payload (e.g., 100 kt), total energy of the device is calculated in Joules using the specific internal energy of TNT. The specific internal energy of nodes is then calculated by dividing the total energy by the nodal mass. The specific internal energy calculated is an input to the simulation as an initial condition. This method produces an isotropic explosion, converting a fraction of its internal energy to kinetic energy, which will be coupled to the target body. Material properties are governed by Tillotson equation of state throughout the simulation for both target body and the explosive device. The Tillotson equation was also used in the in-house GPU SPH algorithm, but is not yet implemented in the CPR method.
- **JWL Equation with a Detonation Mechanism:** A specific detonation mechanism (point source or line source) along with an initiation time governs the energy distribution and coupling. The Jones-Wilkins-Lee equation of state governs the material properties of the expanding high density gas. This gas cloud contains detonation by-products. These simulations and explosion models were tested with multiple material models representing the target body.

The results will be used in calculating an efficiency factor for a subsurface explosion compared to a surface blast. The 20 times efficiency factor was extracted from a study published by National Research Council (NRC) based on a series of tests conducted by the Department of Energy [22]. According to the empirical curves presented in Figure 3.1, subsurface detonations yield an increase to the energy coupling efficiency when compared to surface blasts. The scaled depth-of-burst (DOB) used in Figure 3.1 is defined as

$$DOB = \frac{x}{Y^{(\frac{1}{3})}} \quad (3.1)$$

where  $x$  is the buried depth and  $Y$  is the device yield.

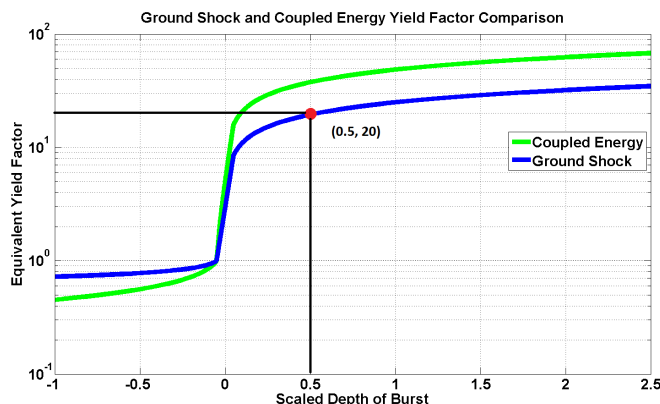


Figure 3.1 Efficiency plot

Validating the above mentioned efficiency factors will aid us in the design process when determining the required impact velocity for the kinetic impactor and required mass of the detonation payload, thus improving overall mission efficiency.

Energy coupling to the target object is determined by the following factors: material characteristics of the target, target resolution, blast modeling scheme and simulation framework (e.g., FEM/SPH), and buried depth of the explosive device [17].

### 3.1.2 Material Modeling

A multitude of material modeling options consisting of different equations of states, strength, and failure models are under investigation in order to capture the accurate material characteristics during the hypervelocity impact and nuclear sub-surface explosion. The NED yield is currently modeled via TNT material properties. The Jones-Wilkins-Lee (JWL) equation of state is specified for the explosive material, while the target is modeled by the Tillotson equation of state. Capturing the material behavior is crucial, as these characteristics determine the failure method, particle velocities, and energy coupling factors. Such parameters can be used to determine appropriate guidance parameters (e.g., impact angle and location) and the orbit determination of HAIV spacecraft. Sections below provide an overview of some equations of state that are currently under test.

### 3.1.2.1 Jones-Wilkins-Lee (JWL) Equation of State.

This equation was developed from various empirical relationships obtained from experiments conducted with high energy explosives such as TNT. Pressure of the explosive gas is given by

$$p = A\left(1 - \frac{\omega\eta}{R_1}\right)e^{-\frac{R_1}{\eta}} + B\left(1 - \frac{\omega\eta}{R_2}\right)e^{-\frac{R_2}{\eta}} + \omega\eta\rho_0 E \quad (3.2)$$

where  $A, B, R_1, R_2$  and  $\omega$  are coefficients obtained from experiments and  $\eta$  represents density ratio between the gaseous products and original material. Specific internal energy of the material is denoted by  $E$ , and  $\rho_0$  is the initial density of the material. A graphical representation of the relationship between pressure and volume is given in Figure 3.2 [2].

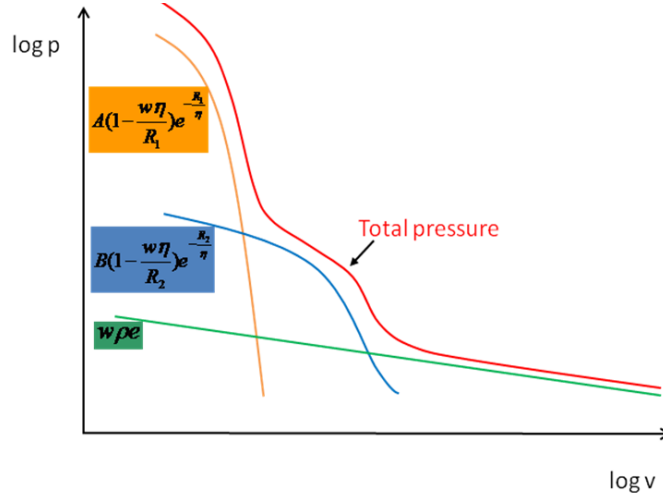


Figure 3.2 JWL equation of state

### 3.1.2.2 Shock Equation of State.

The shock equation of state was developed under empirical relations. The equation represents characteristics of underwater explosions. Definitions of parameters and respective values for water are given in Table 3.1, along with the pressure calculation described by

$$p = \frac{\rho_0 C^2 \mu [1 + (1 - \frac{\gamma_0}{2})\mu - \frac{a}{2}\mu^2]}{[1 - (S_1 - 1)\mu - S_2 \frac{\mu^2}{\mu+1} - S_3 \frac{\mu^3}{(\mu+1)^2}]^2} + (\gamma_0 + a\mu)e \quad (3.3)$$

where  $\mu = \frac{\rho}{\rho_0} - 1$ .

The shock equation of state can also be expressed in polynomial form. This form of the equation of state can also be used in simulations for robust and accurate solutions.

Table 3.1 Shock equation of state properties

Parameter	Definition	Water
$\rho_0$	Initial Density	1000 $kg/m^3$
C	Sound Speed	18.0 (GPa)
$\gamma_0$	Gruneisen coefficient	0.5
a	Volume correction coefficient	0.0
$S_1$	Fitting coefficient	2.56
$S_2$	Fitting coefficient	1.986
$S_3$	Fitting coefficient	1.2268

## 3.2 Algorithm Validation

### 3.2.1 Detonation of 1D Bar of TNT (AUTODYN)

A 1D bar of TNT was detonated at the middle, allowing the shock to propagate symmetrically to the end of the explosive device. Pressure, velocity, and density were recorded from the axis of symmetry to the end of the bar at 14 microseconds simulation time. The simulation setup is shown in Figure 3.3.

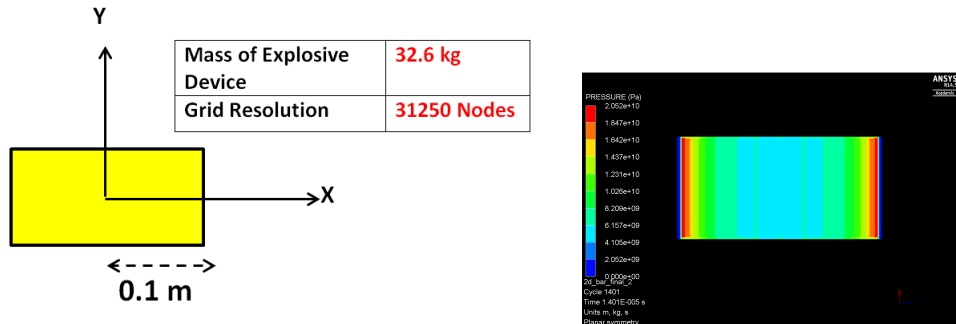


Figure 3.3 1D TNT bar geometry and the pressure solutions at 14 microseconds

Pressure, density, velocity and internal energy results extracted from the AUTODYN solution given above are compared with the SPH results [1]. Comparisons of results are given in Figure 3.4.

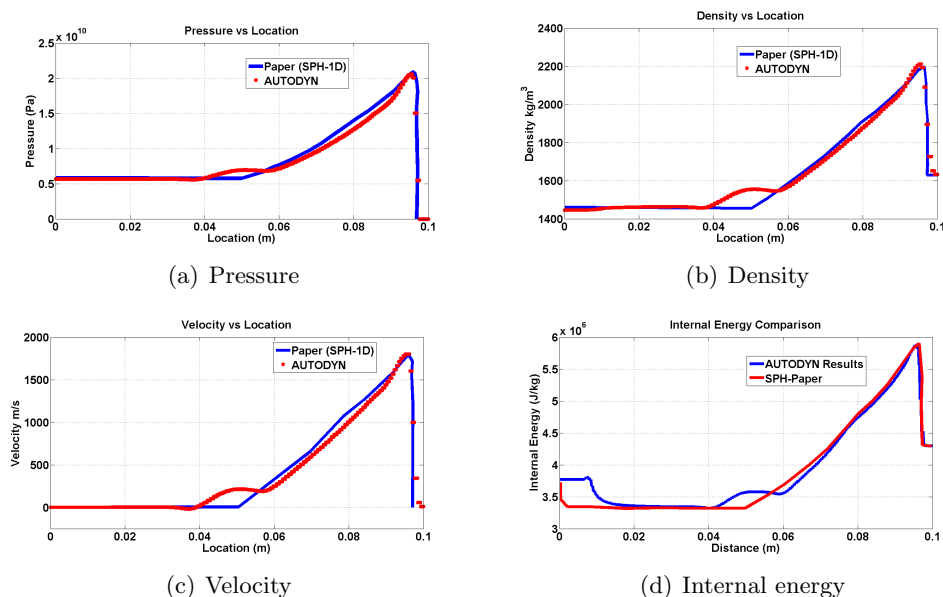


Figure 3.4 1D TNT simulation

Simulated results agree with the curves presented in the paper in a very satisfactory manner. A small peak can be observed in all plots in Figure 3.4 where the change in slope occurs. This could be due to a modeling difference (grid resolution or smoothing length) that can only be identified by comparing both algorithms.

In the absence of another material interface, the shock wave reflects from the edges and travels towards the center of the device. Total energy in the explosive remains as internal energy during the initial shock propagation. During the second stage of the detonation process, most of the internal energy transforms into kinetic energy due to rapid gas expansion. In the presence of another material, such as water, air or rock, the shock wave travels to the material, where a refraction wave occurs, whose magnitude depends on refraction index of the given material. The shock wave may deteriorate depending on the material characteristics, and some of the shock energy is lost through material interfaces and in fragmentation.

### 3.2.2 Underwater Explosion Simulations (UNDEX)

Water was introduced as a material interface in order to compare energy coupling results. Pressure data were obtained through a gauge point located at  $x = 0.25$  m.

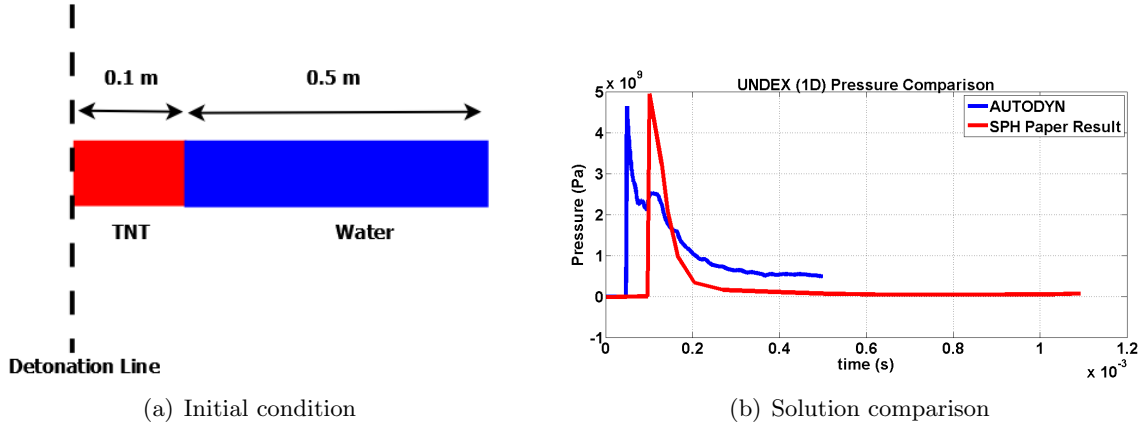


Figure 3.5 UNDEX 1D setup

A simulation setup and a pressure solution are provided in Figure 3.5.

Results obtained from AUTODYN show a 0.5 ms lead. This lead was observable for both material models for water. This could be due to certain modeling schemes such as material boundary treatments and variable smoothing length schemes. An impact separation scheme and a variable scheme can be implemented in AUTODYN, but this makes the simulations prone to numerical instabilities. Implementation of a sound contact algorithm solves most of the lead-lag issues but introduces some stagnation in the material interfaces. Applying penalty schemes also improve material interface treatments.

A 2D axial symmetric simulation was completed as shown in Figure 3.6. The axis of symmetry is shown as a dash line. Gauge points were set to record pressure history. The Mie-Gruneisen equation of state (EOS) was implemented to represent water. Recorded pressure response from the AUTODYN solution is compared with experimental results along with solutions obtained from another SPH algorithm [18].

The 2D planar solver supplied with ANSYS is also used to obtain solutions, analogous to cross sections of a 3D solution extruded towards the  $z$  axis. In order to validate the accuracy of the planar solver a 2D UNDEX simulation was setup using the planar solver as depicted in Figure 3.7. Two gauge points were set above the explosive to record the pressure wave propagation at two different times.

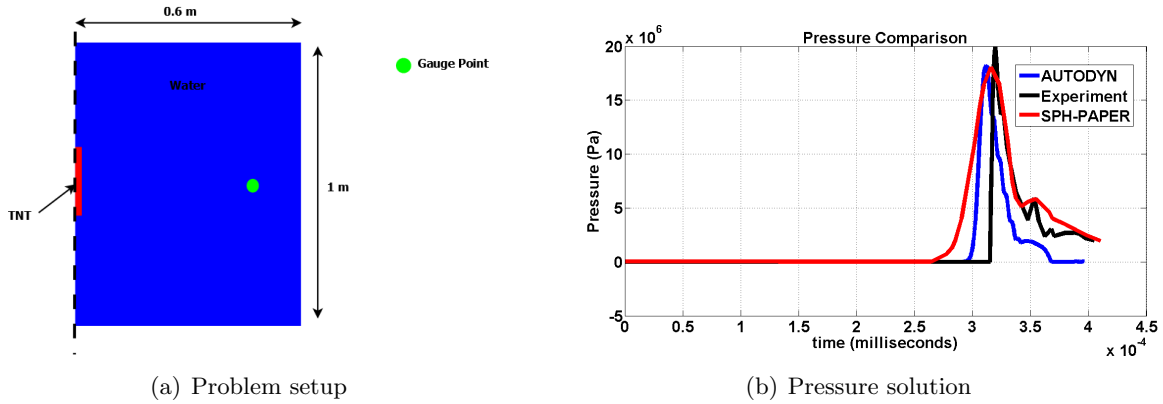


Figure 3.6 UNDEX 2D axisymmetric Solver

A time history of energy coupling from the explosive device to water was also recorded to observe the energy equilibrium status.

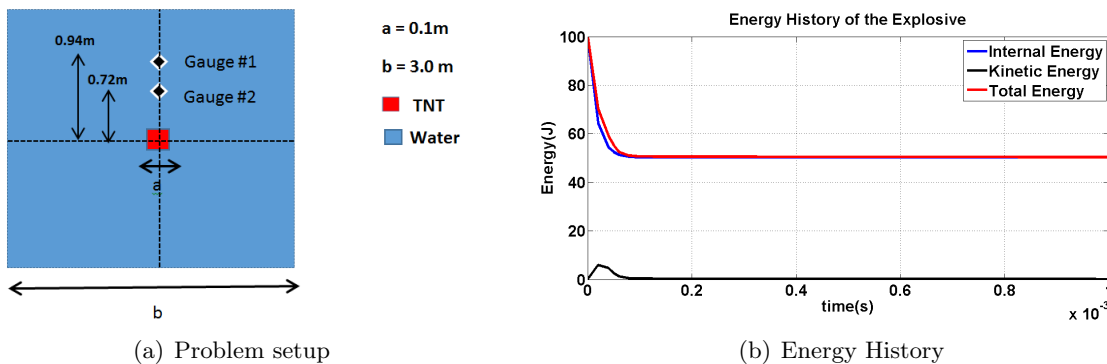


Figure 3.7 UNDEX 2D planar solver

Pressure solutions obtained (Figure 3.8) were compared with the analytical solutions calculated from Zamyshlyayev empirical formulas [9]. The smoothing length had to be kept constant throughout the simulation as the native variable smoothing length scheme resulted in over-predicted results. Upon observing the results, it is clearly understood that the pressure solutions closely agree with the analytical predictions. Discrepancies observed in the shock location or the pressure magnitude may be caused by absence of viscous terms and inherent energy errors. The energy of the explosive particles seems to have decreased to 50% of its original value.

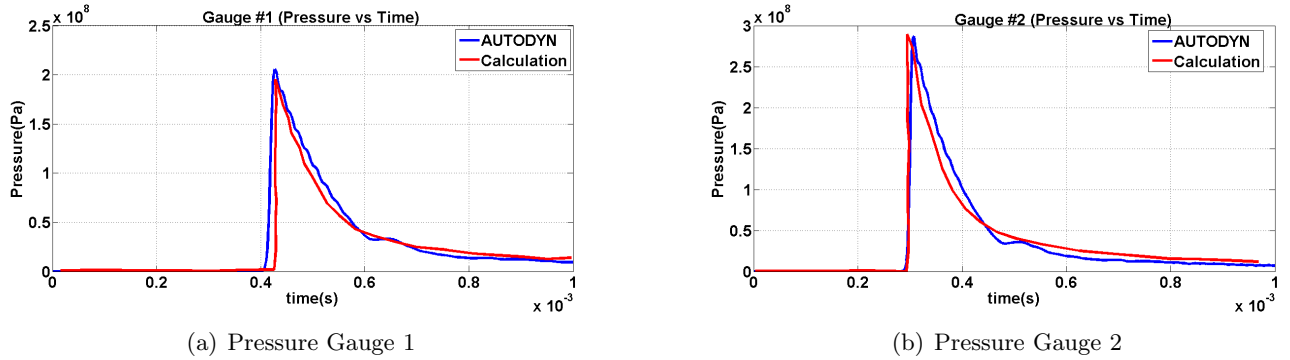


Figure 3.8 UNDEX 2D planar solver - pressure solutions

The simulation has achieved steady state as the energy transfer from TNT to water settles at roughly 50%. This suggests a converged solution and an accurate modeling.

### 3.3 PRELIMINARY RESULTS AND ANALYSIS

#### 3.3.1 2D Planar Simulations (JWL)

2D planar simulations were conducted for sub-surface and contact explosions. The explosive mass was 1.25 tons, governed by JWL equation of state, with a granite material target whose material parameters were governed by the Tillotson equation of state. The simulation setup is shown in Figure 3.9 [25].

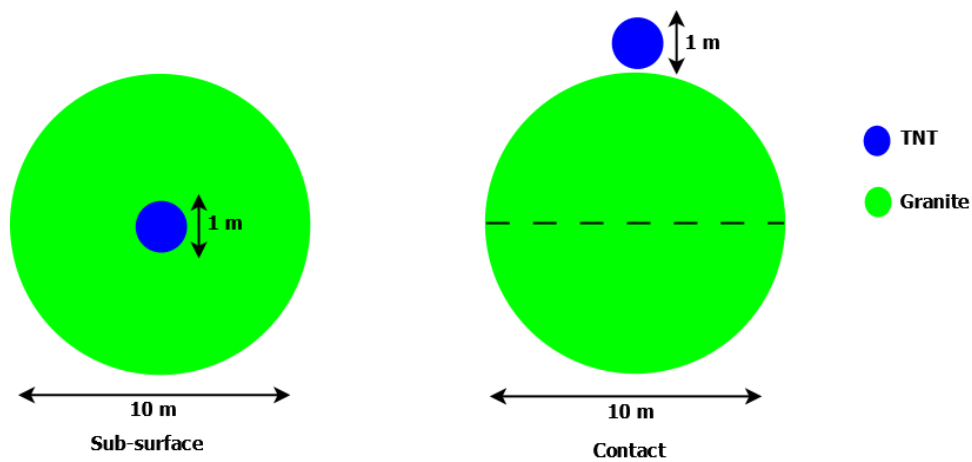


Figure 3.9 Planar simulation setup

The material properties of granite and TNT are given in Table 3.2. AUTODYN material libraries were used to obtain TNT characteristics provided in Table 3.3. Granite parameters were obtained from Marinova et al. [19].

Table 3.2 Tillotson equation of state properties

Parameter	Granite
A	18.0(GPa)
B	18.0 (GPa)
a	0.5
b	1.3
$\alpha$	5.0
$\beta$	5.0
$e_0$	16.0 MJ/kg
$e_s$	3.5 MJ/kg
$e'_s$	18.0 MJ/kg

Table 3.3 JWL equation of state properties

Parameter	Value
A	373.77(GPa)
B	3.7471(GPa)
R1	4.15
R2	0.9
$\omega$	0.35
C-J Detonation velocity	6930 m/s
C-J Energy per unit volume	6(GJ/m <sup>3</sup> )
C-J Pressure	21 (GPa)

Pressure solutions obtained from the AUTODYN simulations are presented in Figure 3.10.

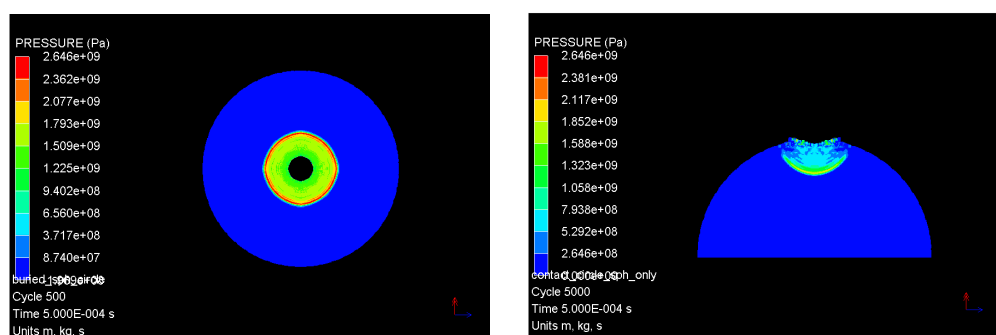


Figure 3.10 Subsurface (left) and contact (right) simulation pressure solution (JWL)

Once the device is triggered, explosive chemical energy, initially stored as internal energy, converts into kinetic energy, generating an isotropic displacement pattern. Percentages of this energy conversions are given in Table 3.4. The JWL model consists of a trigger time along

with a point source detonation and assumes gaseous behavior (ideal gas) for the end products of the detonation, creating a rapid expansion. A point source was placed in the middle of the device as particles and an initial shock wave propagating from the center was observed upon triggering the device. Energy coupling to the target from the explosive device was compared between contact and subsurface explosion cases.

Table 3.4 Subsurface vs contact - JWL

Simulation scenario	Kinetic Energy %	Internal Energy %	Total Energy Transferred %
Subsurface	46.0	54.0	47.0
contact explosion	50.0	50.0	7.0

The explosive efficiency of the subsurface explosion compared to contact explosion scenario was computed to be around 7X.

### 3.3.2 2D Planar Simulations (DED)

These simulations consisted of a spherical target constructed from granite, modeled by the Tillotson equation of state. For the direct energy deposition method, a 1.25 ton device was modeled as high energy granite particles, still governed by Tillotson equation of state. A subsurface explosion with the device buried at the center of the target was simulated which was followed by a simulation of detonating the device slightly above the surface of the target. Pressure solutions for both subsurface and contact simulations are shown in Figure 3.11 [25].

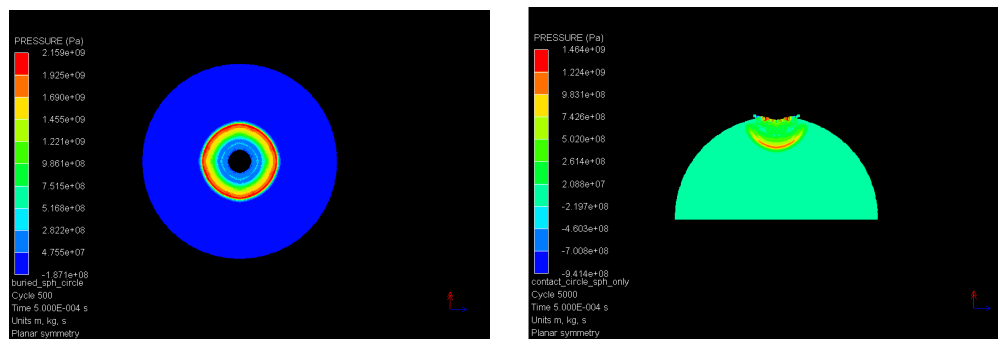


Figure 3.11 Subsurface (left) and contact (right) simulation pressure solutions (DED)

Energy coupling percentages were obtained for the granite target and presented in Table 3.5.

Table 3.5 Subsurface vs contact (DED)

Simulation Scenario	Kinetic Energy %	Internal Energy %	Total Energy Transferred from Explosives %
Subsurface	47.5	52.5	26
Contact Burst	53.7	46.3	3

Energy coupling from direct energy deposition is significantly lower than the coupling factors obtained by using JWL. Overall efficiency between sub-surface and contact simulations for DED method seems to be around 9X.

### 3.3.3 2D Axial Symmetric Solver

An axial symmetry solver was utilized to generate representative 3D solutions for the 2D planar simulations. Both contact and sub-surface explosion simulations used JWL and DED detonation models. Pressure solutions for JWL are shown in Figure 3.12, while the DED solutions are in Figure 3.13. Energy coupling factors with respect to the total yield of the device for both cases are presented in Table 3.6 [25].

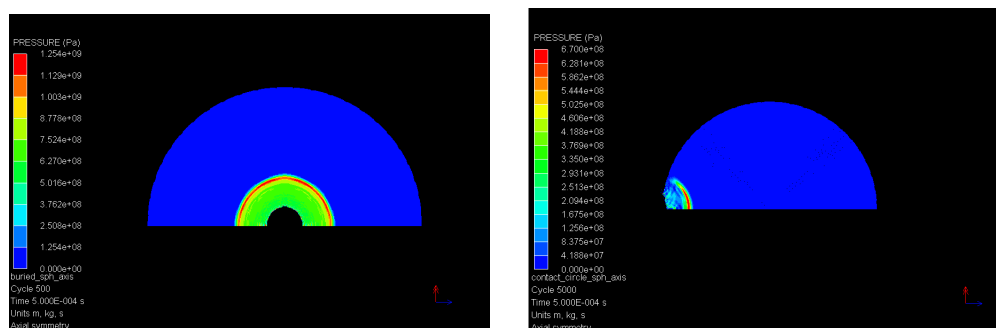


Figure 3.12 2D Axial symmetry (JWL): subsurface (left) and contact(right) pressure solutions

Table 3.6 Subsurface vs contact - Axial symmetric

Simulation scenario	Kinetic Energy %	Internal Energy %	Total Energy Transferred from NED %
Subsurface (JWL)	53.2	46.8	55.4
contact explosion (JWL)	47	53	4.75
Subsurface (DED)	46.9	53.1	23.3
contact explosion (DED)	47	53	2

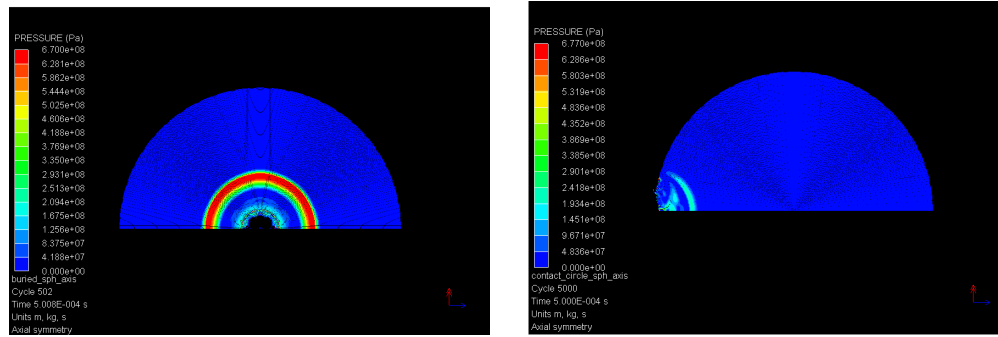


Figure 3.13 2D Axial symmetry (DED): subsurface (left) and contact (right) pressure solutions

For the subsurface explosion that utilizes JWL model, 46.8% of the total energy coupled to the asteroid remained as internal energy, while 53.2% caused nodal displacement as kinetic energy. A significant amount of energy (45% from the initial yield) remained in the explosive nodes as internal energy. As per the corresponding contact burst, 53% of the total energy coupled remained as internal energy. About 95% of the total yield of the device remained in the explosive particles as internal energy for the contact blast simulation. Efficiency of the subsurface blast with respect to contact explosion is computed to be 12X.

As predicted in the 2D planar simulation, energy coupling seems to be significantly low for DED (axial symmetric) simulations when compared to the JWL simulations. The majority (roughly 73%) of the total yield of the device remained in the designated explosive nodes for the subsurface explosion, while 98% of the device energy didn't couple to the target during the contact blast. The explosive efficiency was calculated to be 12X.

According to these simulations, a significant percentage of energy remains in the explosive device. However, in an actual nuclear blast or a conventional explosive usage, a significant portion of total energy (35% to 45%) turns into thermal radiation [20]. The SPH framework employed by AUTODYN lacks thermal radiation modeling and therefore most of the energy in the explosive device remains in the assigned particles as internal energy. However, the JWL explosion model seems to be predicting higher energy coupling factors and efficiencies when compared to the direct energy deposition method.

### 3.4 Conclusions

The AUTODYN software demonstrates the ability to solve the problems as posted in this paper. Simulations under JWL explosion modeling showed higher energy coupling to the target bodies when compared against the direct energy deposition methods. More research is required to better understand the modeling differences between these two methods. Based on data comparison plots obtained in many cases, it can be concluded that the JWL model should be used in modeling high explosive simulations.

Future work is desired in understanding the modeling of the energy coupling and transfer to a target body through JWL models and energy sourcing. Different strength and material models should also be investigated, specifically rubble or porous materials. From multi-dimensional simulations, a comprehensive grid study should be completed to better understand the relationship between energy coupling and grid resolution.

## CHAPTER 4. Thermal Shield Development

In this section, I discuss the development of a simple thermal shield to protect the follower vehicle carrying the NED payload from the heat flux radiated from the super-heated particles of the crater. The super hot particles are caused by the initial impact between the asteroid and the kinetic impactor. An algorithm was developed to solve these problems with a range of assumptions. The algorithm contains four stages, as follows

- **Stage 1** : Predicting Temperature of the crater
- **Stage 2** : Calculating the temperature on the surface of NED
- **Stage 3** : Predicting temperature distribution inside the NED
- **Stage 4** : Determining materials suitable to withstand extreme temperatures

This algorithm was developed to obtain steady state solutions as they provide with the worst case survivability scenarios for the thermal shield. These estimates will improve in future with the introduction of a time integrated algorithm.

### 4.1 Stage 1

During the stage 1 development, a simple algorithm was developed which utilizes the output from the in-house GPU accelerated SPH method. This was later replaced with direct temperature output obtained from ANSYS AUTODYN. In this step, temperatures of all the particles will be estimated as a secondary calculation by using the data gathered from a SPH run. Internal energy ( $U$ ), density ( $d$ ) and mass ( $m$ ) will be extracted from the output of SPH algorithm.

Temperature of the  $i^{th}$  particle is given by

$$T_{\text{final}} = T_{\text{initial}} + \frac{\Delta U}{C_{v(\text{mean})}} \quad (4.1)$$

where  $C_{v(\text{mean})}$ , heat capacity of a constant volume, is calculated using a weighted average of  $C_v$  and density of asteroid material. Both  $C_v$  and  $C_p$  are equal for solid materials. The derivation of  $C_v$  is shown below. As the simulation assumes the mass to be constant before and after the initial collision, conservation of mass can be applied as

$$\sum_{i=1}^N m_i = \text{Constant} \quad (4.2)$$

The conservation of mass can be rewritten assuming constant volume ( $V$ ) for each particle as

$$\sum_{i=1}^N \rho_i V = \sum_{i=1}^n m_i \quad (4.3)$$

Therefore, volume of a particle can be redefined as

$$V = \frac{\sum_{i=1}^n m_i}{\sum_{i=1}^n \rho_i} \quad (4.4)$$

By using the Einstein equation for solids,  $C_v$  for each particle can be calculated by [21].

$$C_v(i) = 3N_i k_B \quad (4.5)$$

where  $N_i$  is defined as  $N_i = \frac{\rho_i V}{\text{molar mass}} \times (\text{Avagadro Number})$  and the Boltzmann constant is represented by  $k_B$ . Using the information presented above, A  $C_{v(\text{mean})}$  value can be predicted with the help of a weighted average:

$$C_{v(\text{mean})} = \frac{\sum_{i=1}^n C_v(i) \rho_i}{\sum_{i=1}^n \rho_i} \quad (4.6)$$

An array of assumptions were also made in order to make the calculation process simple and fast. The secondary space craft was assumed to be made out of aluminum. Phase changes

that occur in asteroid materials during the initial impact were not taken into account. Initial temperatures of all the SPH nodes were set to zero while the temperature changes across the shock wave propagation was also ignored.

A sample temperature prediction for the newly created crater of a 70 m asymmetric asteroid is shown in Figure 4.1. This geometry was used in Chapter 2 for a sensitivity study.

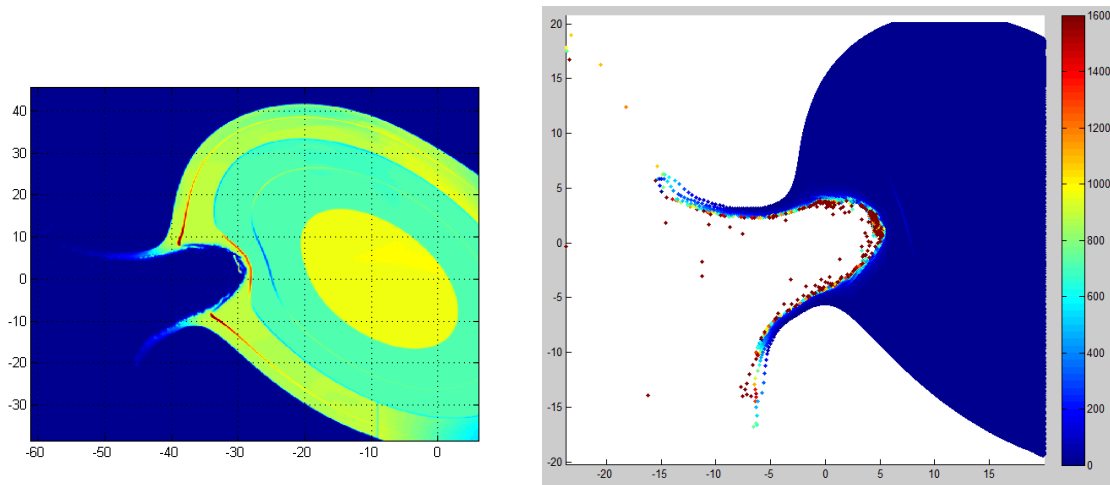


Figure 4.1 Nodal density (left) and temperature in Kelvin (right)

Upon observing Figure 4.1, super-heated particles can be seen concentrated on the bottom of the crater. They are also present inside the crater traveling at arbitrary directions which could potentially hit and damage a Whipple shield or melt the payload upon contact.

## 4.2 Stage 2

After the crater temperatures have been predicted, another section of the algorithm was created to calculate view factors for each side of the spacecraft. The view factors are defined as groups of super-heated particles in the crater which contributes to the heat flux each side of the payload experience. A sample diagram in Figure 4.2 shows the each side of the spacecraft with respect to the crater.

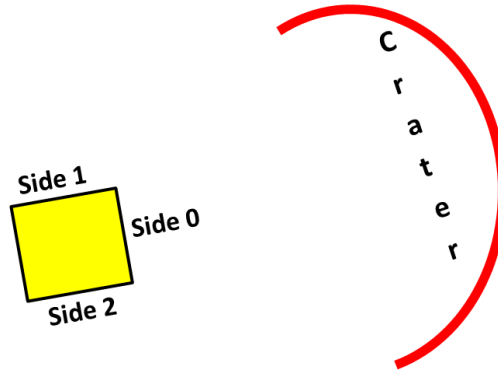


Figure 4.2 Sides of the spacecraft

Once the view factors are determined, heat flux calculations can be performed using a steady state thermal equilibrium assumption. In order to calculate the heat radiated from the crater and the heat absorbed by the aluminum spacecraft, solid angles ( $\Omega$ ) for each view factor were calculated.

Figure 4.3 illustrates the how the heat is radiated to the side of the spacecraft using the solid angle. The solid angle was defined as the angle created between each heated particle and the corresponding side of the follower vehicle.

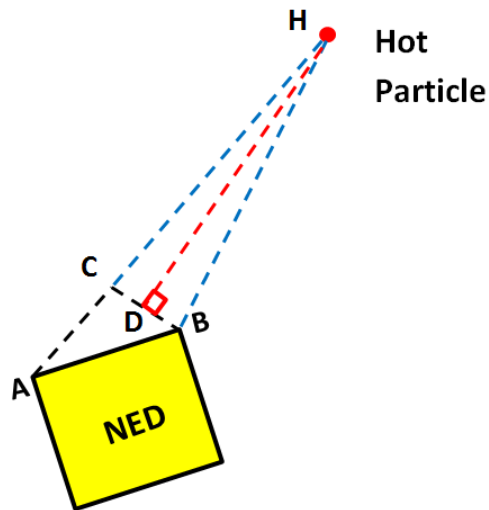


Figure 4.3 Solid angle calculation

A 1 m height was assumed for the spacecraft. The distances indicated in blue (HC and HB) are equal in magnitude. If the length HD is defined as  $r$  and the length BC is defined as  $l$ , the solid angle can be calculated by:

$$\Omega = \frac{l}{r^2} \quad (4.7)$$

The thermal radiation emitted from the heated asteroid material and received by aluminum walled spacecraft is calculated using the heat radiation transport theory [14]. The temperature of each side of the NED payload is given by

$$\alpha_r \sum_{i=1}^N (\Omega_i \epsilon_e \sigma T_{e(i)}^4) = \epsilon_r \sigma T_r^4 \quad (4.8)$$

where  $\alpha_r$  is the absorption coefficient of the spacecraft material. Emissivity of the receiver (spacecraft wall) and the emissivity of the heat flux emitter (super heated asteroid particles) are denoted by  $\epsilon_r$  and  $\epsilon_e$ . The temperature on the surface of the spacecraft is given by  $T_r$  while the temperature of the heat emitting node is given by  $T_e$  where N number of particles are affecting a respective wall of the NED. The Stefan-Boltzmann constant is given by  $\sigma$ .

### 4.3 Stage 3

Once the temperatures of the spacecraft walls were established for the steady state condition, this information was fed to a heat diffusion model to evaluate the 2D temperature distribution inside the follower vehicle for a time scale of a 1.0 millisecond assuming the impactor and the NED are separated by a 10 m distance while traveling at 10 km/s. A simple explicit scheme was introduced to solve the thermal diffusion equation given by

$$\frac{\partial T}{\partial t} - c \nabla^2 T = 0 \quad (4.9)$$

where temperature (T) is the diffusing property for a material volume with  $c$  thermal conductivity. Once a  $\Delta x$  discretization and a  $\Delta t$  time step are specified, the stability criterion is given by [15]

$$K = \frac{\alpha \Delta t}{\Delta x^2} \leq \frac{1}{2} \quad (4.10)$$

The explicit finite difference representation of the discretized 1D equation is given below. Index of the node is denoted by  $i$  and the current time step is represented by  $n$ .

$$T_i^{n+1} = T_i^n + K (T_{i+1}^n - 2T_i^n + T_{i-1}^n) \quad (4.11)$$

### 4.3.1 Validation of Explicit Heat Diffusion

A sample validation was conducted to ensure the accurate implementation of the explicit scheme. The following time dependent heat distribution was used as an example [15].

$$T(x, t) = \sin\left(\frac{\pi x}{L}\right) e^{-\frac{\alpha \pi^2 t}{L^2}} \quad (4.12)$$

where  $L$  was the total length of the discretized length. Temperatures at  $x = 0$  and  $x = L$  boundaries were set to zero, while the initial temperature distribution across the length was given by

$$T(x) = \sin\left(\frac{\pi x}{L}\right) \quad (4.13)$$

The constructed explicit scheme was run until  $t = 1.0s$  and the results from both exact solution and the explicit scheme were compared in Figure 4.4.

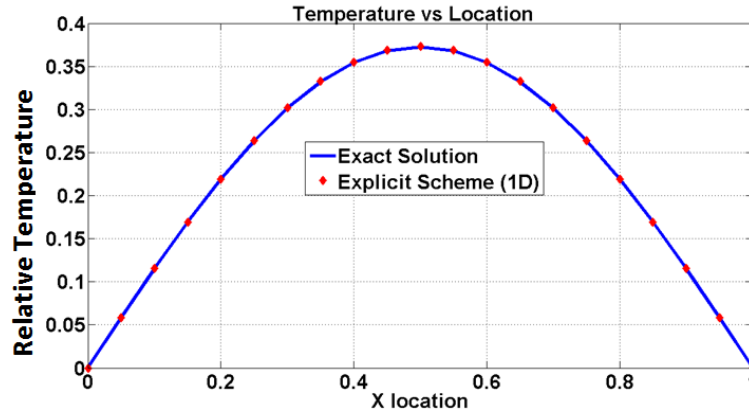


Figure 4.4 Heat diffusion validation result

The validation shown in Figure 4.4 demonstrates the accuracy of implementation of the explicit solver scheme. The explicit scheme is computationally less expensive and stable. However obtaining solutions in high resolution grids requires decreasing the time step for a stable

run. In order to increase the accuracy of thermal modeling, the explicit algorithm was extended to a 2D representation as given in:

$$T_i^{n+1} = T_i^n + K_x (T_{i+1}^n - 2T_i^n + T_{i-1}^n) + K_y (T_{i+1}^n - 2T_i^n + T_{i-1}^n) \quad (4.14)$$

where  $K_x$  and  $K_y$  are defined as:

$$\begin{aligned} K_x &= \frac{\alpha \Delta t}{\Delta x^2} \leq \frac{1}{2} \\ K_y &= \frac{\alpha \Delta t}{\Delta y^2} \leq \frac{1}{2} \end{aligned} \quad (4.15)$$

. This model is currently used in the radiation heat transfer algorithm and the boundary conditions are determined by the temperatures of the outer walls of the secondary space vehicle. Final construction of the algorithm is given in Figure 4.5.

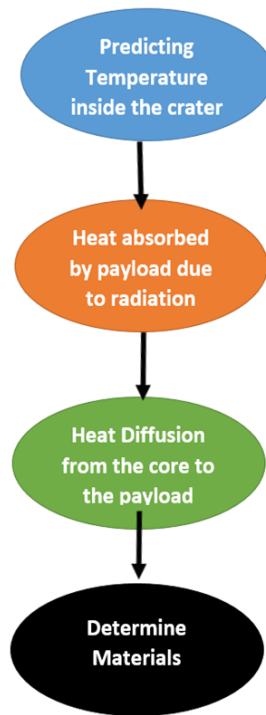


Figure 4.5 Final construction of the algorithm

#### 4.4 Stage 4

After obtaining the temperature distribution inside the secondary vehicle, the need for a thermal protection shield was recognized. As an initial step, a list of materials that can withstand extreme temperatures was compiled. Some of the materials identified as potential candidates for heat shields through industry recommendations are given in Table 4.1.

Table 4.1 Material properties

Material	Conductivity (W/(mk))	Melting Point (K)	Boiling Point (K)
Aluminum	237	933.47	2797
Tungsten	173	3695	5828
Tantalum	57.5	3290	5731
Tantalum Carbide	22.0	4153.15	5053.15
Graphite	5.7	4000	4500
Titanium	21.9	1941	3560
Hafnium Oxide (Ceramic)	23.0	3030	5673

These material were recommended by the researchers at the Ames Laboratory of Iowa State University. They are currently used in many extreme thermal applications ranging from turbine blades to re-entry heat shields where the materials are coated on to surfaces using industrial techniques. These coatings were applied to surfaces via a plasma gun and the ceramics such as Hafnium Oxide are never layered above a metallic layer as it may crack during expansion. The design requirement for the thermal shield demands a survival time of 1.0 millisecond. The initial iteration of the secondary vehicle utilized a metallic thermal shield which will later be improved with better temperature approximations.

#### 4.5 Design Process - Example

A sample case was constructed to test the design process. The old temperature prediction algorithm was revamped to accept temperature output from AUTODYN. A new sample case was constructed and solved in AUTODYN where an Al impactor collides with a Granite spherical target at 10 km/s. The follower vehicle was assumed to have a square cross section with temperature predictions obtained at  $x = -10.0$  m. The initial setup along with a thermal distribution is shown in Figure 4.6.

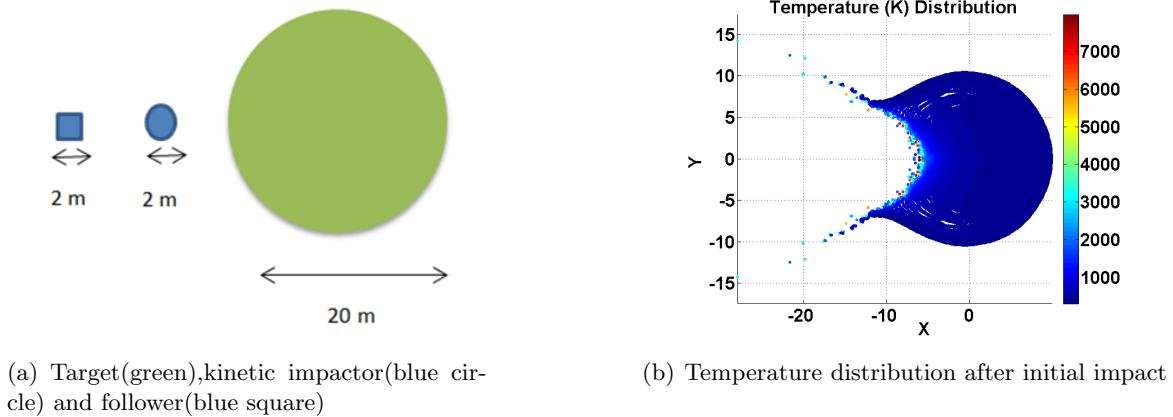


Figure 4.6 Thermal test setup and temperature distribution

View factors were calculated for side 0, 1 and 2 (see Figure 4.2). This determines the amount of heated particles which affects each side of the spacecraft. The aft of the spacecraft is neglected as it is not subjected to heat radiation for the most part of its journey towards the crater. Sub-figures shown in Figure 4.7 and Figure 4.8 show how each region is defined and the location of the particles they “see”. The temperatures below 1500 K were omitted as molten rock temperatures are above 1500 K.

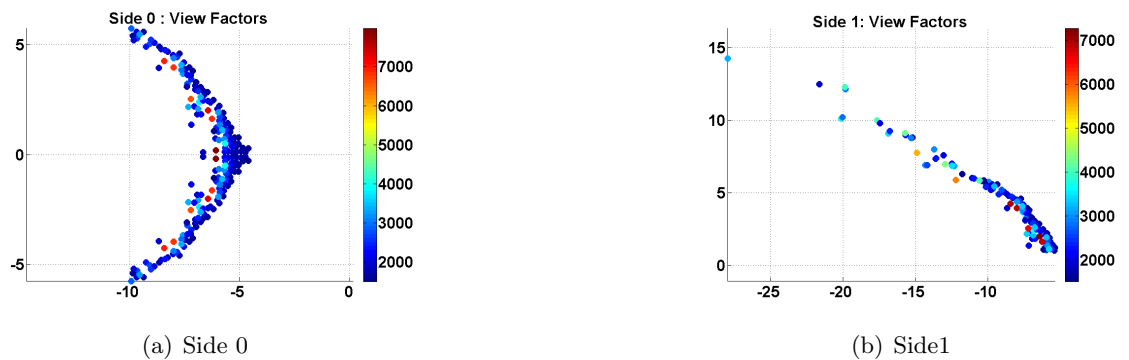


Figure 4.7 View factor calculations - side 0 and side 1

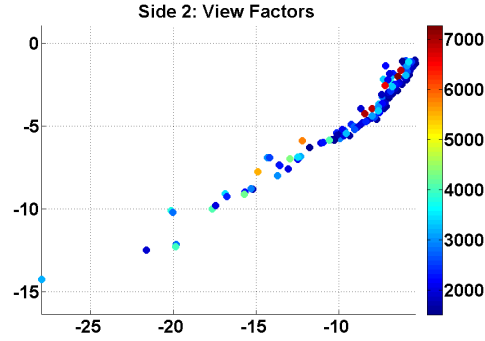


Figure 4.8 View factor calculations - side 2

After obtaining the temperatures of the crater particles and determining particles each side of the spacecraft see (view factors), the algorithm calculates the temperatures on the spacecraft sides or regions. The emissivity and the absorptivity of aluminum was found to be 0.02 and 0.08 [26]. Emissivity of granite was obtained as 0.45 [27]. The temperatures are given in Table 4.2.

Table 4.2 Temperatures of each side

Side	Temperature (K)
Side 0	9100.2
Side 1	6592.3
Side 2	6592.3

The results have portrayed the trends we have seen in the older version of the algorithm. Side 0 has the highest temperature as it directly faces the hot surface of the crater. Side 1 and Side 2 have identical temperatures. This is caused by the symmetry of the results and the symmetrical placement of the follower on x axis. Side 1 and 2 experience a lower temperature than side 0 as the number of particles affecting those sides is significantly lower than the particles affecting side 0. Based on the temperatures predicted on the surface of the NED, the temperature diffusion inside the NED is given in Figure 4.9.

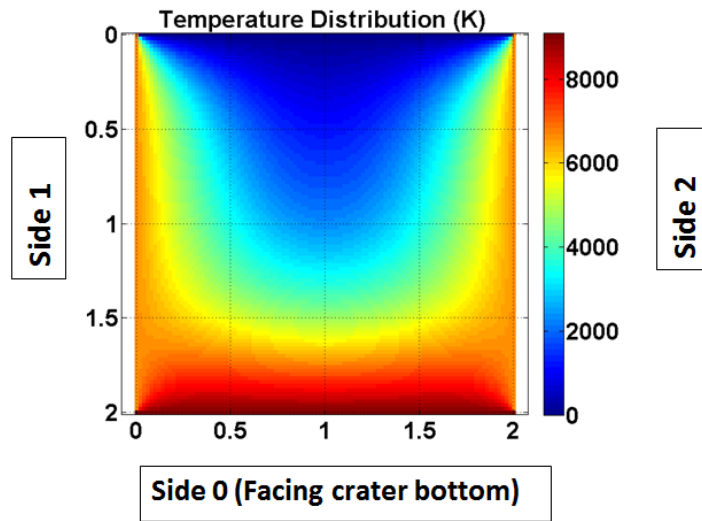


Figure 4.9 Temperature diffusion - aluminum

According to materials provided in Table 4.1 it is proven that the aluminum wouldn't sustain these temperatures as the shield reaches melting temperatures. A layer of tungsten was decided to be sprayed on the aluminum to withstand the extreme temperatures that will be burned off as the follower vehicle travels towards the crater. Based on the information acquired from researchers at Ames Laboratory, a 0.2 mm thick tungsten layer was chosen. This adds an additional mass of 50.0 kg to the mass of the secondary vehicle. This mass is subjected to vary with future research on lighter materials and better temperature approximations.

## CHAPTER 5. Whipple Shield Development

A Whipple shield is used in many modern day spacecraft to protect the structure from orbital debris and micro meteoroids. It is designed to sustain impact velocities ranging from 3-18 km/s. A Whipple shield consists of a relatively thin outer bumper made from metal or composite (Nextel/Kevlar) placed some distance away from the inner wall of the space craft. A test setup is given in Figure 5.1. This setup will be later reconstructed in AUTODYN for simulation purposes and the MLI (Multi Layer Insulation) will be removed from the simulation setup.

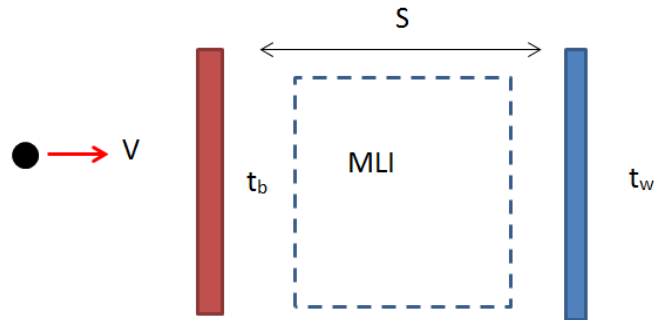


Figure 5.1 Whipple shield setup

The front bumper is shown in red and its thickness is given by  $t_b$ . The bumper come into contact with meteoroid debris and other particles traveling at hypervelocities. The wall of the spacecraft is shown in blue and its thickness is given by  $t_w$ . The distance between the bumper and the wall is denoted by  $S$ .

## 5.1 Ballistic Limit Equations (BLE)

Ballistic limit equations define the threshold particle diameter that could cause perforation/spall of the inner wall. These equations do not always provide the correct predictions due to their empirical nature. These equations were constructed via analyzing data from various hypervelocity lab tests. The inaccuracies in predictions are caused by material defects, non-homogeneous density distributions and other failure modes. Ballistic limit equations are defined for 3 regions based on a material phase change and failure after the kinetic impact. These equations were developed by NASA Johnson Space Center [11].

- Ballistic Phase ( $V < 3.0$  km/s) : The projectile or the micro-meteoroid debris penetrates without breaking into pieces. The equation for the maximum particle diameter ( $d_c$ ) is given by

$$d_c = \left( \frac{t_w \left(\frac{\sigma}{40}\right)^{0.5} + t_b}{0.6 \cos(\theta)^{\frac{5}{3}} \rho_p^{0.5} V^{\frac{2}{3}}} \right)^{\frac{18}{19}} \quad (5.1)$$

- Shatter Phase ( $3.0$  km/s  $< V < 7.0$  km/s) : The projectile breaks and creates an expanding debris cloud upon impacting the front bumper.

$$d_c = \left\{ \left( \frac{t_w \left(\frac{\sigma}{40}\right)^{0.5} + t_b}{1.248 \cos(\theta)^{\frac{5}{3}} \rho_p^{0.5}} \right)^{\frac{18}{19}} \left(1.75 - \frac{V \cos(\theta)}{4}\right) \right\} + \left\{ [1.071 t_w^{\frac{2}{3}} \rho_p^{-\frac{1}{3}} \rho_b^{-\frac{1}{9}} S^{\frac{1}{3}} \left(\frac{\sigma}{70}\right)^{\frac{1}{3}}] \left(\frac{V \cos(\theta)}{4} - 0.75\right) \right\} \quad (5.2)$$

- Melting Phase ( $V > 7.0$  km/s) : As the projectile hits the bumper both materials will melt and vaporize due to the vast amounts of kinetic energy transfer. This relationship is given in:

$$d_c = 3.918 t_w^{\frac{2}{3}} \rho_p^{-\frac{1}{3}} \rho_b^{-\frac{1}{9}} (V \cos(\theta))^{\frac{-2}{3}} S^{\frac{1}{3}} \left(\frac{\sigma}{70}\right)^{\frac{1}{3}} \quad (5.3)$$

where the density of the bumper and wall are given by  $\rho_b$  and  $\rho_p$ . Rear wall yield stress is given by  $\sigma$ . The impact angle  $\theta$  is measured from a x axis defined normal to the bumper shield.

A sample BLE curve is shown in Figure 5.2 for a wall thickness of 0.16 cm and a bumper thickness of 0.16 cm. The shield was assumed to be constructed of aluminum alloy which has a yield stress of 37 ksi. The separation between the wall and the bumper is 12.0 cm.

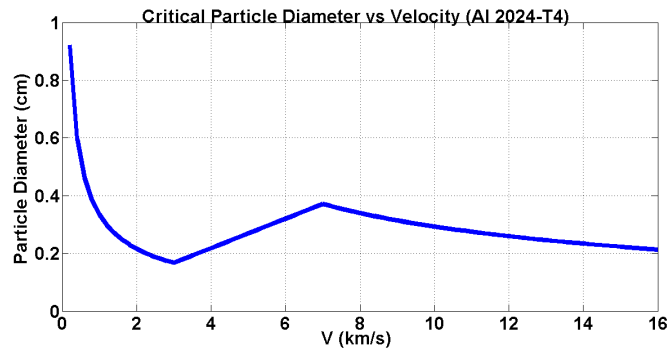


Figure 5.2 BLE curve

The Figure 5.2 clearly shows different traits for different velocity regions. The velocity region between 3 km/s and 7 km/s is observed to be linear. In an actual Whipple shield design scenario, the curve is used to make the following predictions:

- If the diameter of the debris (assuming spherical debris) exceeds the critical diameter for a given impact velocity ( $V$ ), that results in rear wall perforation.
- If the diameter of the debris is below the critical limit for a given impact velocity ( $V$ ), that ensures the safety of the rear wall (spacecraft wall). No material loss will be predicted.

To observe the trends in BLE curves with varying parameters, the original wall thickness ( $t_w$ ) was doubled (0.32 cm) and tripled (0.48 cm). Increasing the wall thickness, improves the structural integrity of the spacecraft wall as fast moving debris has to penetrate more layers of the material. Therefore, an increase in critical particle diameter is bound to occur for each velocity station. The Figure 5.3 depicts change in critical diameter for different thicknesses (0.16, 0.32, 0.48 cm) of the rear wall. Critical diameter curves seem to have shifted upwards as the wall thickness increases. This qualitative trend validates the relationship between critical particle diameter (for a given velocity) requirement and the spacecraft wall thickness.

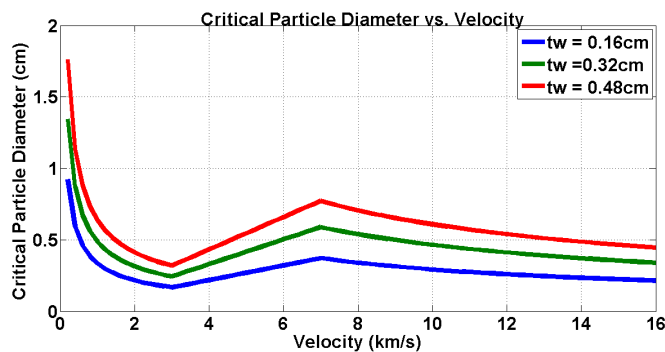


Figure 5.3 Wall thickness comparison

## 5.2 Validation of Whipple Shield Design Process

In order to utilize AUTODYN 2D in an actual Whipple shield design loop, it was used to reproduce some results available through the literature. The input parameters included a shock equation of state followed by strength modeling done using Johnson-Cook strength model. The axial symmetry solver was used in this case to generate the results. A qualitative comparison was performed for solutions obtained at different times during the progression of the solution. The projectile had an impact velocity of 3.1 km/s colliding normally to the bumper shield. The bumper thickness was set to 2.0 mm. Both the bumper and the projectile were modeled using the SPH method which was later coupled with a finite element approach that represented the spacecraft wall. The spacecraft wall was 10.0 mm thick and located 200 mm away from the bumper shield. The bumper and the rear wall were made out of Al 2024 while the projectile was constructed out of Al 1100. The input for the equation of state is given in Table 5.1 and Table 5.2 [12].

Table 5.1 Shock EOS : Al-2024 and Al-1100

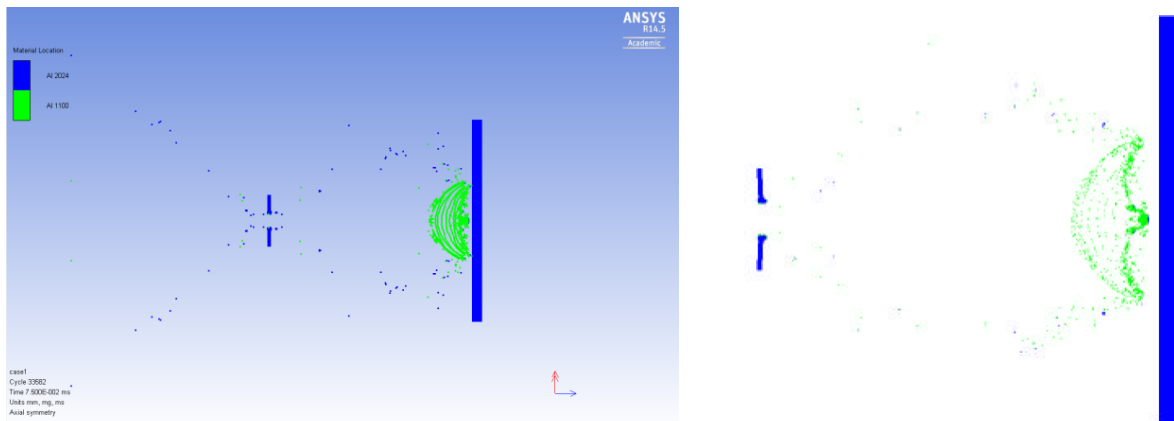
Parameter	Units	Value
Density (Al-2024/Al-1100)	$kg/m^3$	2785/2701
Bulk sound Speed	$ms^{-1}$	53258
$\gamma_0$	Gruneisen coefficient	0.5
Particle Shock velocity slope	N/A	1.338
Specific Heat Capacity	$Jkg^{-1}K^{-1}$	875

Table 5.2 Johnson-Cook : Al-2024 and Al-1100

Parameter	Units	Value
Yield Stress	GPa	0.265
Shear Modulus	GPa	27.6
Hardening Constant	GPa	0.426
Hardening Exponent	N/A	0.34
Strain Rate Constant	N/A	0.015
Thermal Exponent	N/A	1.0
Melting Temperature	K	775

A Principal Stress failure model was also incorporated with max tensile stress of 2.5 GPa and 1.0 GPa for Al 2024 and Al 1100 respectively. An Erosion option was also turned on to counter any cell degeneration that exceeded an instantaneous geometric strain of 1.0. The rear wall had a fixed boundary condition at 73 mm from the radial locations.

A set of qualitative solutions obtained during specific time instances are shown in Figure 5.4 and Figure 5.5. These were compared with the solutions available in [12] for further validation.

Figure 5.4 Nodal displacement  $75\mu s$ : AUTODYN solution (left) and literature solution (right)

In a qualitative comparison to the results presented in the literature, the AUTODYN solutions show identical dispersion patterns. Both solutions suggest successful operation of the Whipple shield as the inner wall only got slightly dented by the impact. Slight changes in the debris cloud can be observed along with changes in deformation. These could be due to certain modifications the AUTODYN solver underwent in the span of 10+ years since the recorded simulation.

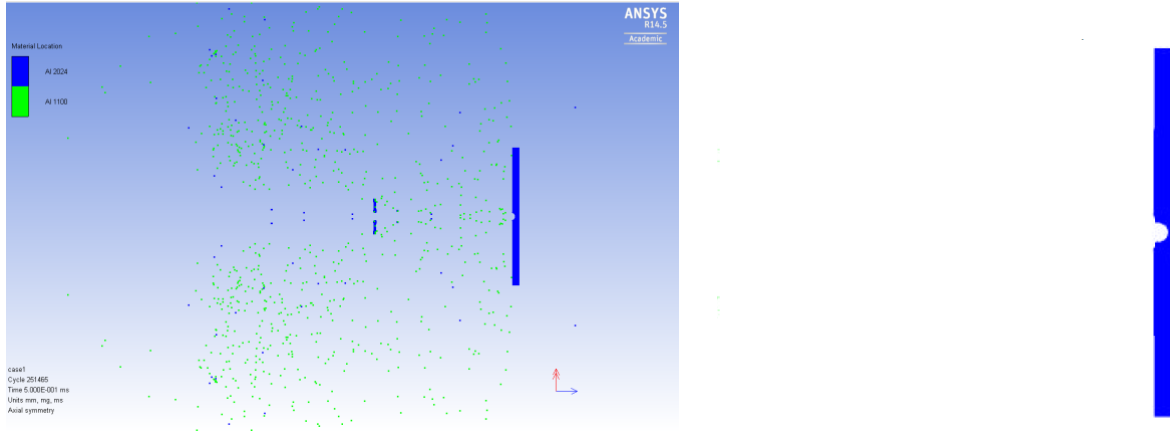


Figure 5.5 Nodal displacement  $500\mu s$ : AUTODYN solution (left) and literature solution (right)

The initial location of the impactor was not recorded in the literature work so I placed it 1 mm away from the bumper assuming the initial analyst tried to keep it close as possible to the bumper to avoid unnecessary simulation time. Geometrical trends observed in the debris cloud and the plate deformations seem to be accurate. Results were mirrored along x axis to obtain the axisymmetric solution of the simulation.

### 5.3 Whipple Shield - Validation 2

A series of test cases were simulated in order to validate the methodology under experiment. The results were based on gas gun experiments which were later validated by using AUTODYN 2D and PAMSHOCK 3D [13]. The complete test scenario was modeled by using the SPH method for AUTODYN 2D and the PAMSHOCK model contained a rear wall that was modeled in FEM. Method I have used in this validation consists of a 3D Lagrangian-Lagrangian coupled system which consists of a projectile that is modeled in SPH and two walls that obey solid mechanics in a FEM framework. A shock EOS along with Johnson-Cook strength model were used in all these cases utilizing Al-2024 alloy for the bumper, wall and the projectile. Anticipated perforation results are tabulated in Table 5.3 [13].

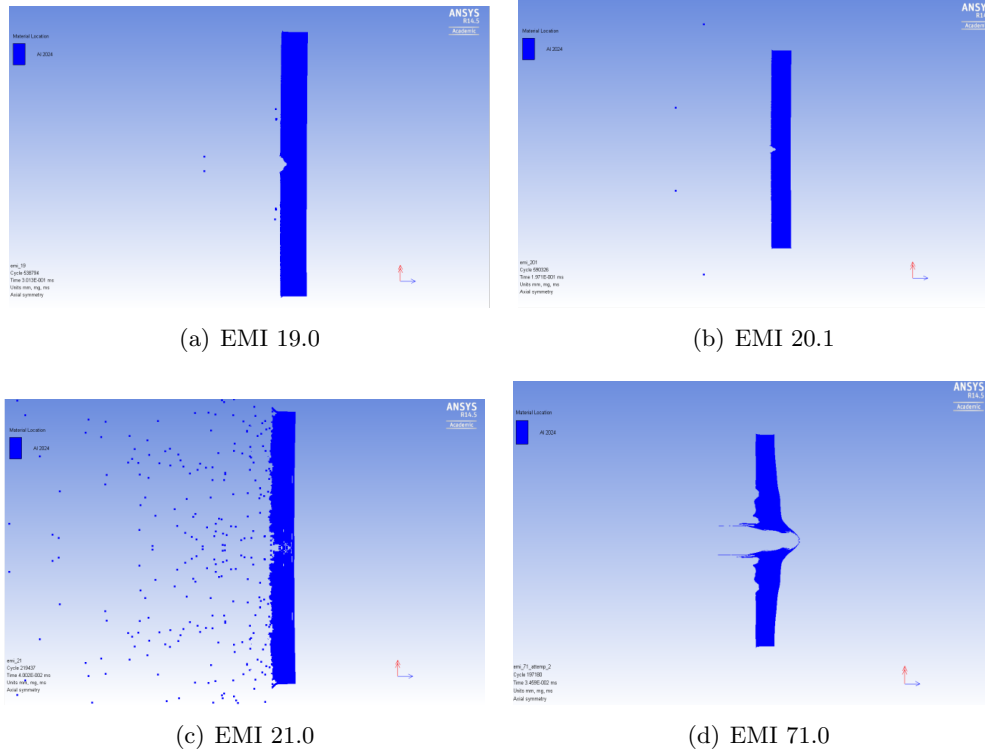


Figure 5.6 Results - validation 2

Table 5.3 Whipple validation results

Test No.	Velocity (km/s)	Projectile Diameter(mm)	$t_b$ (mm)	$t_w$ (mm)	Expected Result
EMI 19.0	3.31	5.0	1.6	3.2	NP
EMI 20.1	5.5	5.0	1.6	3.2	NP
EMI 21.0	7.2	5.0	1.6	3.2	NP
EMI 71.0	5.1	8.0	1.6	3.2	P

Perforation of the Whipple shield is denoted by "P" and the No Perforation is denoted by "NP" in column 6 of Table 5.3. These cases were run with axisymmetric solver. Each case consisted of a projectile and a bumper shield modeled in SPH along with a rear wall that is captured by a Lagrangian grid. Cells in the Lagrangian grid were set to deteriorate for a given effective plane strain. Qualitative results are shown in Figure 5.3. The cases seem to be producing the anticipated results. EMI 19, 20.1 and 21.0 have shown no perforation while EMI 71 is showing clear perforation. Even though the results accurately predict the perforation of a given case, it does not match up with the images provided in literature. This may be due to changes in the solver and different material parameters and options the authors have used in

the process that were undocumented. These cases will be re-run in future to determine possible causes.

### 5.3.1 Whipple Shield for HAIV

The Whipple shield that will be implemented in the HAIV will be constructed out of aluminum due to its strength. The shield will protect the space craft from debris traveling up to 10 km/s. The maximum diameter of the debris should be 5 mm. Once an algorithm that predicts the debris size is developed, a better approximation for the bumper and wall thickness can be obtained. A Calculation of the mass of the Whipple shield is performed assuming the dimensions of the spacecraft given in in Figure 5.7.

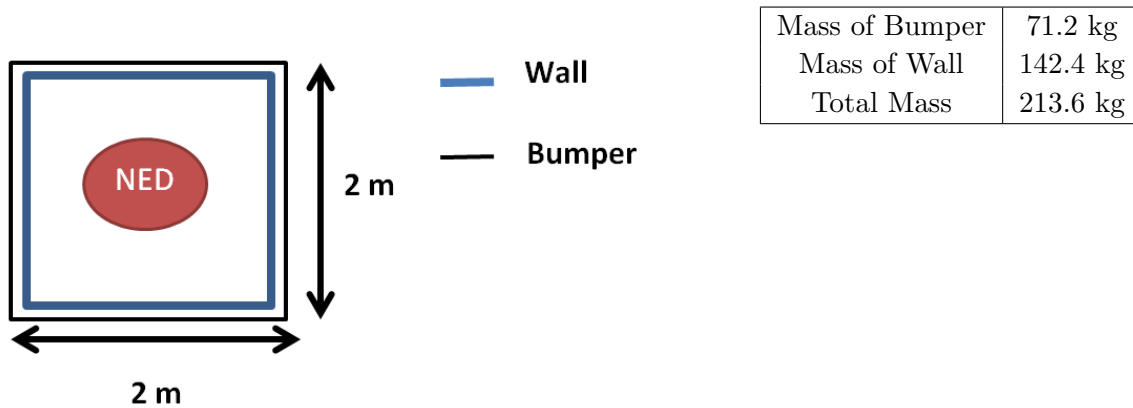


Figure 5.7 Whipple shield - HAIV

## CHAPTER 6. Future Work

This chapter discusses certain future developments of the current research topics which was elaborated in this thesis so far. Research to improve current blast optimization work is currently being tested in new frameworks while different solver models are being tested, validated and modified to encapsulate maximum physical characteristics such as material failure, fragmentation and energy coupling. Thermal and Whipple shield topics will also be further expanded with better physical coupling and further research in material modeling related to the development of composites.

### 6.1 Blast Modeling

A new computational fluid dynamics algorithm is being developed at ADRC by Ben Zimmerman to simulate blast waves from high energy sources. This solver method, Correction Procedure using Reconstruction(CPR) is a higher order algorithm that solves shock wave propagation through a user defined grid [25]. Initial developments of this algorithm is geared towards simulating blast waves in ideal gas which will later be expanded to a multi-material blast solver with fragmentation. In order to support the ongoing research with the CPR method, AUTODYN's Eulerian grid based solver will be used instead of the SPH solver. This Eulerian multi-material solver is currently used in the industry to simulate a variety of explosion scenarios. This solver can be coupled with Finite Element Method(FEM) to measure structural deformations. However, the AUTODYN Euler solver has demonstrated instabilities that leads to large energy errors upon introducing high energy sources.

### 6.1.1 Sod's Shock Tube

A simple shock tube validation was performed to validate the grid based Euler multi-material solver in AUTODYN. The explosive device was represented as a high pressure gas and the surrounding area was under relatively low pressure. Material properties were governed by the following form of ideal gas equation [16].

$$P = (\gamma - 1)\rho E \quad (6.1)$$

which defines pressure ( $P$ ) as a relationship between adiabatic index ( $\gamma$ ), density ( $\rho$ ) and specific internal energy ( $E$ ). A 400 X 400 grid space was declared as the domain of calculation with a 0.8m diameter circular high pressure gas region at the center. Initial conditions for both explosive device and the surrounding gas are given in Table 6.1.

Table 6.1 Ideal gas properties

Parameter	Explosive	Surrounding
Pressure	1.0 Pa	0.1 Pa
Density	1.0 $kg/m^3$	0.125 $kg/m^3$
Mass	0.5 kg	0.44 kg

The simulation was run for 0.25 seconds as a planar simulation and a 2D pressure solution was obtained. The case setup and pressure solution is provided in Figure 6.1.

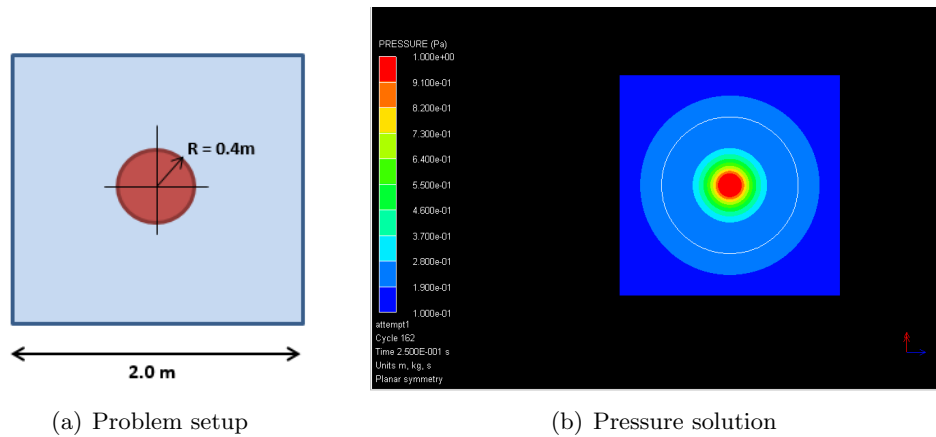


Figure 6.1 Sod's shock tube solution

A shock wave appears to be propagating outwards through the surrounding material triggered by the pressure difference indicated in Table 6.1. However this shock wave doesn't appear to be carrying a significant amount of energy at the shock front as observed in simulation results from Chapter 3. The material interface between high pressure gas and the surrounding gas can be seen as a thin white line suggesting an expanding bubble like behavior. Pressure, density, specific internal energy and velocity solutions were extracted along the x axis starting from the center of the explosion and ending at the boundary. These results were compared with the simulation results obtained in literature [16] and the recently developed CPR blast solver as shown in Figure 6.2.

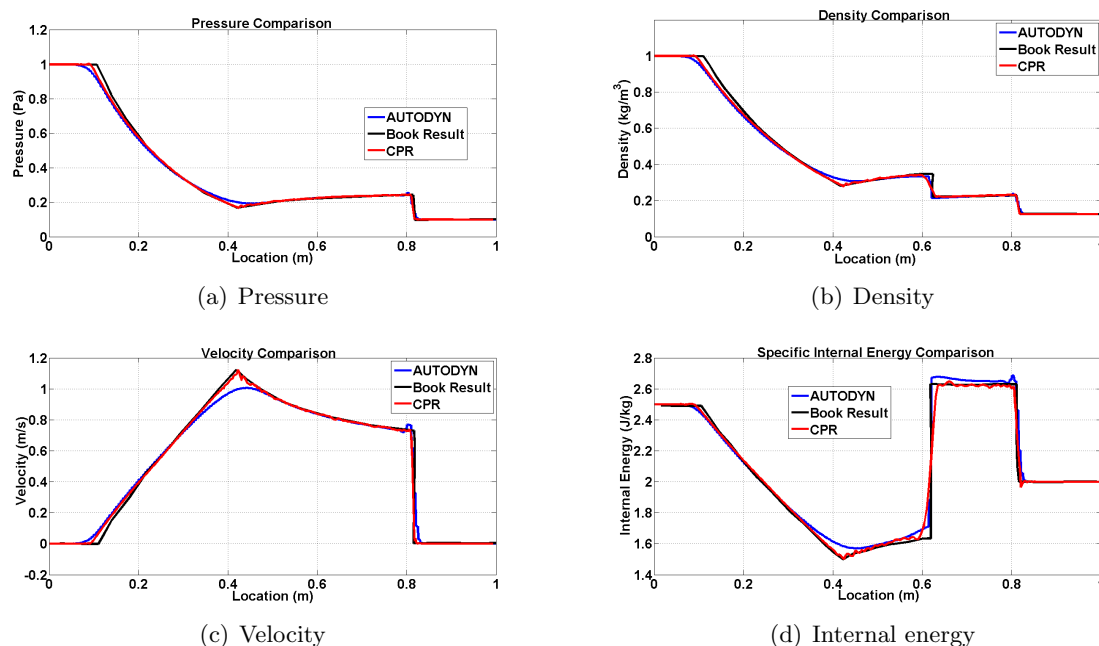


Figure 6.2 Comparison of results - Sod's shock tube

Both the CPR method and AUTODYN solutions generally agree with the solutions provided in literature. The CPR method shows a slight oscillatory behavior that is native to higher order methods. However, the CPR method was very successful in capturing the inflection points in both specific internal energy and velocity comparisons. AUTODYN solution seems to have smoothed out in those sharp corners which may be alleviated by using a highly refined grid or a user defined limiter.

### 6.1.2 Taylor-Sedov Blast Wave

As the development behind the CPR method is ultimately purposed towards nuclear detonation simulations, a Taylor-Sedov blast wave can be set as an appropriate benchmark case. This case encapsulates many characteristics of a high energy simulation including a shock wave with a large instant pressure magnitude. A Sedov blast wave simulation also reveals flaws in a simulation framework that may be triggered via large energy errors. A sample Sedov blast wave was generated using a energy source with a high energy density with a small volume was introduced to an axisymmetric simulation. A rectangular Cartesian grid was defined with a length of 10 m and a width of 5 m. The spherical explosive device was placed at (5.0,0) with a radius of 0.0875 m. The device contained  $10^5$  J and the entire control volume had an initial density of  $1.0 \text{ kg/m}^3$ . Material properties were governed by the ideal gas equation [29]. A Pressure wave solution obtained at  $t = 0.1 \text{ s}$  is given in Figure 6.3.

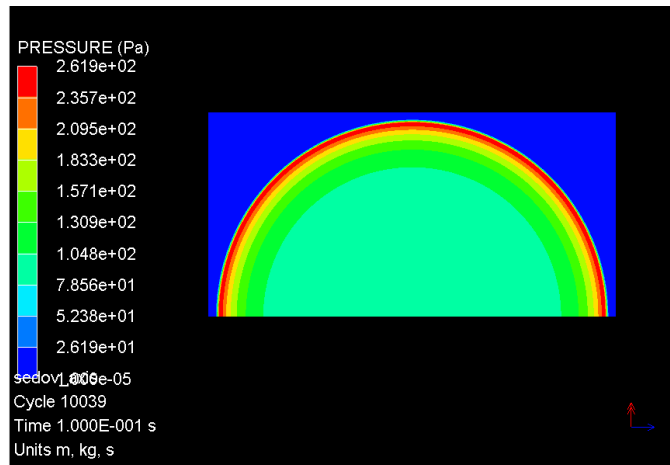


Figure 6.3 Sedov blast wave - pressure solution

At the beginning of the simulation ( $t = \Delta t$ ), a sudden pressure jump of  $10^{12}$  Pa was created. Due to this sudden pressure amplitude, the Eulerian solver seems to have accumulated a large energy error. The AUTODYN simulation was adjusted to ignore the energy error and proceed with the shock wave. Both pressure and density data was extracted along the line,  $x = 5$ . These curves were compared with the corresponding analytical solution.

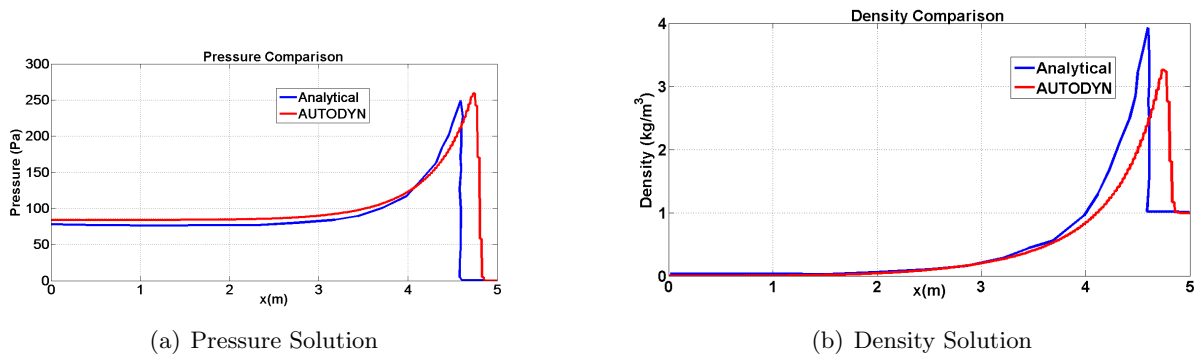


Figure 6.4 Sedov blast wave

The solutions obtained by the simulations (shown in Figure 6.4) were slightly different from the analytic solutions. Both analytical and numerically obtained pressure solutions demonstrated a slight difference in  $x$  location of the peak while density solutions had a slight under prediction. Such differences are possible due to large energy errors and other simulation instabilities. However, these issues will be fixed in the future research with CPR method by introducing limiters and other stabilization criterion.

## 6.2 Thermal and Whipple Shield Development

Both thermal and Whipple shields will be subjected to extensive material testing with the use of AUTODYN. Composites such as Nextel and Kevlar should be tested with accurate material parameters to ensure structural strength. The new grid based CPR method coupled with fragmentation dynamics will allow researchers to determine the average size of a fragment which is crucial in determining Whipple shield thicknesses. A new time dependent heat radiation scheme will be introduced to the current steady state algorithm using COMSOL, a commercial multi-physics software .

## BIBLIOGRAPHY

- [1] Liu, G. R. and Liu, M. B., Smooth Particle Hydrodynamics: a mesh free particle method. World Scientific Publishing Co.Pte.Ltd
- [2] ANSYS, Inc. ANSYS 14.5 Help. ANSYS, Inc, SouthPointe,275 Technology Drive, Canonsburg, PA 15317.
- [10] Wie, B., Hypervelocity Nuclear Interceptors for Asteroid Disruption. *Acta Astronautica*, 90, 146–155, 2013.
- [4] Pitz, A.,Vardaxis, G.,Winkler, T. and Wie, B., Conceptual Design of a Hypervelocity Asteroid Intercept Vehicle (HAIV) and Its Flight Validation Mission. *Acta Astronautica*, 94, 42–56, 2014.
- [5] Barbee, B., Wie, B., Steiner, M., and Getzandanner, K., Conceptual Design of HAIV Flight Demonstration Mission. *AIAA-2013-4544, AIAA Guidance, Navigation, and Control Conference, Boston, MA. 2013.*
- [6] Kaplinger, B., Premaratne, P.D., Setzer, C. and Wie, B., GPU-Accelerated 3D Modeling and Simulation of a Blended Kinetic Impact and Nuclear Subsurface Explosion. *AIAA-2013-4548, AIAA Guidance, Navigation, and Control Conference Boston, MA, 2013.*
- [7] Liu, M.B., Liu, G.R., Zong, Z., Lam, K.Y., Computer simulation of high explosive explosion using smoothed particle hydrodynamics methodology. *Computers and Fluids*, 32,305–322, 2003.

- [8] Borve, S., Bjerke, A., Omang, M., Svinsas E., A Comparison of AUTODYN and RSPH on Two-dimensional Shock Waves Problems. *Norwegian Defense Research Establishment*, 2009.
- [9] A-man, Z., Wen-shan Y., Xiong-liang Y., Numerical Simulation of Underwater Contact Explosion. *Applied Ocean Research*, 340,10–20, 2012.
- [10] Wie, B., Hypervelocity Nuclear Interceptors for Asteroid Disruption. *Acta Astronautica*, 90, 146–155, 2013.
- [11] Piekutowski, A. J., Poormon, K.L., Christiansen, E.L., Davis, B.A., Performance of Whipple Shields at Impact Velocities above 9 km/s. *International Journal of Impact Engineering*, 38, 495–503, 2011.
- [12] Hayhurst, C.J., Livingston, I.H., Clegg, R.A., Fairlie, G.E., Hiermaier, S.J., Lambert, M., Numerical Simulation of Hypervelocity Impacts on Aluminum and Nextel/Kevlar Whipple Shields. *Hypervelocity Shielding Workshop*, 1998.
- [13] Palmieri, D., Faraud M., Destefanis, R., Marchetti, M., Whipple Shield Ballistic Limit at Impact Velocities Higher than 7 km/s. *International Journal of Impact Engineering*, 26, 579–590, 2001.
- [14] Gray, W.A., Muller, R., Engineering Calculations in Radiative Heat Transfer. *Pergamon Press Ltd.*, 1974.
- [15] Recktenwald, G.W., Finite-Difference Approximations to the Heat Equation. 2011.
- [16] Toro, E., F., *Riemann Solvers and Numerical Methods for Fluid Dynamics : A Practical Introduction*.
- [17] Gurjicic, M., Pandurangan, B., & Cheeseman, B.A., A Computational Analysis of Detonation of Buried Mines. *Multidiscipline Modeling in Materials and Structures*, 2, 363–388, 2006.

- [18] Zhang, A., Yang, W., Huang, C., & Ming, F., Numerical Simulation of Column Charge Underwater Explosion based on SPH and BEM Combination. *Computers and Fluids*, 71, 169–178, 2013.
- [19] Marinova, M.M., Aharonson, O., Asphaug, E., Geophysical Consequences of Planetary-Scale Impacts into a Mars-like Planet. *Icarus*, 211, 960–985, 2011.
- [20] Pentagon et al., *The Military Critical Technologies List (Part II)*, Department of Defense, 1400 Defense Pentagon, Washington, DC 20301. 1998.
- [21] Rogers, D., *Einstein's Other Theory: The Planck-Bose-Einstein Theory of Heat Capacity*, Princeton University Press, 2005.
- [22] *Effects of Nuclear Earth-Penetrator and Other Weapons*, National Academy of Sciences, 2005.
- [23] Kaplinger, B., Wie, B., Dearborn, D. Nuclear Fragmentation/Dispersion Modeling and Simulation of Hazardous Near Earth Objects. *Acta Astronautica*, 90, 156–164, 2013.
- [24] Xu., J., Liu, X., Analysis of structural response under blast loads using the coupled SPH-FEM approach. *Jzus- Sci A*, 9, 1184–1192, 2008.
- [25] Premaratne, P., Zimmerman, B., Setzer, C., Harry, J., Wie, B., Nuclear Explosion Energy Coupling Models for Optimal Fragmentation of Asteroids. *AAS 14-285, AAS Conference*, New Mexico, January-2014.
- [26] Henninger, J. H., Solar Absorptance and Thermal Emittance of Some Common Spacecraft Thermal-Control Coatings. *NASA Reference Publication*, 1984.
- [27] Golden, L. M., *Laboratory Experiments in Physics and Modern Astronomy*. Springer, 2012.
- [28] Asphaug, E., Ostro, S.J., Hudson, R.S., Scheeres, D.J., & Benz, W., Disruption of kilometer-sized Asteroids by Energetic Collisions. *Nature*, 393, 437–440, 1998.

- [29] Clarke, D. A., ZEUS 3D. Available online at <http://www.ap.smu.ca/dclarke/zeus3d/3dtest01.html>.  
Date Accessed : 4/24/2013